Advances in Colloid and Interface Science 334 (2024) 103305

Contents lists available at ScienceDirect

Advances in Colloid and Interface Science

journal homepage: www.elsevier.com/locate/cis

Historical Perspective

Droplet evaporation on super liquid-repellent surfaces: A controllable approach for supraparticle fabrication

Xiaojing Wang [a], Yuechang Lian [a], Siyuan Xiang [b], Shengyang Tao [a,*], Michael Kappl [c], Wendong Liu [a,*]

[a] Dalian Key Laboratory of Intelligent Chemistry, School of Chemistry, Dalian University of Technology, Linggong Road 2, Dalian 116024, PR China
[b] Academy of Food Interdisciplinary Science, School of Food Science and Technology, Dalian Polytechnic University, Qinggongyuan 1, Dalian 116034, China
[c] Department of Physics at Interfaces, Max Planck Institute for Polymer Research, Ackermannweg 10, D-55128 Mainz, Germany

ARTICLE INFO

Keywords:
Supraparticles
Evaporation
Assembly
Droplet
Superhydrophobic surface
Lubricant surface

ABSTRACT

Supraparticles are agglomerates of nano- and/or microparticles with sizes ranging from tens to hundreds of microns, making them more accessible for handling and recovery than the building blocks. Supraparticles not only inherit the properties and functions of primary particles but also exhibit characteristics such as high porosity, large specific surface area, and improved functionalities, which can be attributed to the synergism, coupling, and co-localization among the constituents. Therefore, supraparticles hold promising applications in catalysis, drug delivery, sensing, etc. Among the various synthesizing strategies, evaporating droplets on a liquid-repellent surface is proposed as an effective approach to fabricate supraparticles with unique structural features and functions. The boundary conditions of such droplet-confinement methods significantly drive the formation of supraparticles by reducing or avoiding the use of solvents or processing liquids, which further accelerates the development and utilization of supraparticles. This paper presents an overview of recent developments in the fabrication of supraparticles by evaporating droplets on liquid-repellent surfaces. The review focuses on the evaporation processes on lubricant and superhydrophobic surfaces, structural regulation, and applications of supraparticles. Finally, an outlook on the future directions of evaporation on liquid-repellent surfaces mediated supraparticle fabrication is presented.

1. Introduction

Supraparticles are agglomerates formed by primary nano- or microparticles assembly. These primary particles can combine in different types to endow the supraparticles with integrated functionalities or assemble a single component into complex structures [1–6]. As assembled structures, supraparticles alleviate processing difficulties and environmental risks associated with the high mobility of nanoparticles, enhancing material controllability and recyclability. Further, interactions (e.g., synergism, coupling, and colocalization) among the confined constituent particles enable supraparticles to exhibit enhanced properties derived from the primary particles and generate new features (i.e., porosity and large specific surface area) [6,7], highlighting potential applications across various fields [4,8]. The high specific surface area of supraparticles makes them suitable for catalysis and pollutant detection [6,8,9]. A high porosity allows the supraparticles to serve as delivery systems for biological organisms [10]. Further, the assembled structures exhibit enhanced light capture and absorption efficiency, making them applicable in solar cell devices with improved photoelectric conversion efficiency [11].

Based on the structural characteristics of supraparticles and their prospects in different fields, researchers developed a series of assembly/synthesis methods to construct supraparticles with specific structures and functionalities [6,12–15]. These methods are broadly categorized into thermodynamics/kinetics-controlled assembly and template-controlled assembly methods. The former assembles supraparticles through weak interactions (e.g., hydrogen bonding, dipole-dipole interactions, solvophobic interactions) by involving coupling agents, ligands, and oligomers [16–20]. The latter confines the primary particles by utilizing templates, such as emulsions/microemulsions, block copolymers, and microfluidic droplets, and it drives the supraparticle assembly through the subsequent solvent removal [21–24]. Although suitable for large-scale production, aforementioned methods depend greatly on chemicals that generate large amounts of organic wastes,

* Corresponding authors.
E-mail addresses: taosy@dlut.edu.cn (S. Tao), liuwendong@dlut.edu.cn (W. Liu).

https://doi.org/10.1016/j.cis.2024.103305
Received in revised form 23 September 2024;
Available online 30 September 2024

which include solvents, cross-linking agents, and surfactants. Meanwhile, the as-prepared supraparticles require tedious purification treatments, increasing their complexity and energy consumption [25–27]. Therefore, exploiting green supraparticle fabrication strategies with low energy consumption is important for reducing or avoiding the use of organic solvents, emulsifiers, templates, and processing liquids.

In the past decade, evaporation-mediated self-assembly has been proposed as an effective approach for supraparticle fabrication, wherein supraparticles are formed on super-liquid-repellent surfaces (superhydrophobic surfaces and lubricant (−infused) surfaces) [5,28–32]. A deposited water droplet partially wets the surface and forms a spherical cap on general hydrophobic surfaces. During evaporation, the gas-liquid-solid three-phase contact line is mostly pinned, leading to a contact angle below 90° and faster water evaporation near the contact line. Anisotropic evaporation resulted in liquid flows from the center of the droplet towards the contact line, thereby driving the aggregation of primary particles towards the periphery and forming a ring- or donut-shaped structure [15,33,34]. Compared to hydrophobic surfaces, superhydrophobic surfaces have a water contact angle (WCA) that exceeds 150°. Consequently, the contact area between the droplet and the substrate is very small ($\ll V^{2/3}$). The contact line shrinks with droplet evaporation while the droplet remains spherical, thereby forming an almost spherical supraparticle [5,31,35–37]. Although the apparent contact angle is below 150°, water droplet on a lubricant (−infused) surface in a non-wetting state with contact line pinning are eliminated, which can drive the particles inside the droplet to form supraparticles after evaporation. The composition of the initial droplets, interactions between primary particles, evaporation conditions, and external electric/magnetic fields significantly affect the characteristics of as-prepared supraparticles [5,15,32,38–40]. In addition, supraparticles can be obtained without post-processing, and therefore, evaporation-mediated particle assembly on super-liquid-repellent surfaces has been proposed as a green and effective strategy to fabricate supraparticles and promote the application of materials with supraparticles. This review introduces the basic droplet evaporation mechanism on super-liquid-repellent surfaces. An overview of the fabrication and regulation of supraparticles mediated by evaporating dispersion drops on super-liquid-repellent surfaces is provided. Finally, we present representative applications of the as-prepared supraparticles and provide an outlook on the future development directions of evaporation-mediated supraparticle fabrication.

2. Droplet evaporation mechanism on liquid-repellent surfaces

Droplet evaporation plays an essential role in supraparticle formation, with the evaporation behavior directly relying on the surface structure and repellency. The wettability of a surface is controlled by surface chemistry, which determines surface energy, and morphology, which affects roughness. Indeed, the characteristics of a liquid play an essential role in its wetting behavior. A common method to assess surface wettability is through the contact angle (θ) of water droplets deposited on the surface. The contact angle is defined as the angle between the liquid-solid interface and tangent line of the curve at the point of contact between the solid, liquid, and gas phases. The θ value provides insight into how a droplet wets a solid surface. Considering water droplets as an example, surfaces can be divided into superhydrophilic ($\theta < 5^{\circ}$), hydrophilic ($5^{\circ} < \theta < 90^{\circ}$), hydrophobic ($90^{\circ} < \theta < 150^{\circ}$), and superhydrophobic ($\theta > 150^{\circ}$) surfaces [41]. Notably, a material is classified as superhydrophobic when it displays a contact angle exceeding 150°, coupled with a wetting hysteresis of 1–3° and a roll angle of less than 15° upon interaction with an aqueous medium in a thermodynamically stable, non-uniform wetting configuration [42].

Nature is the primary source of various surface/interface structures, as flora and fauna evolved unique surface properties for adapting to the external environment. For example, the protruding structures on lotus leaves enable them to self-clean [43–47], compound eyes of insects prevent fogging and anti-reflection [48,49], and gecko feet exhibit high adhesion due to the specialized surface structures [50,51]. Inspired by these fantastic properties, various biomimicking surface have been constructed and applied in production and life. Super-liquid-repellent surfaces constitute a significant portion of many surfaces/interfaces. Based on the differences in liquid repellency, super-liquid-repellent surfaces can be classified as lubricated, superhydrophobic, superoleophobic, and superamphiphobic surfaces. We uniformly categorize super-liquid-repellent surfaces into superhydrophobic and lubricated surfaces to simplify the system description.

Superhydrophobic surfaces exhibit extreme water repellency. The water droplets do not wet these surfaces and maintain nearly ideal spherical shapes with apparent contact angles greater than 150° and rolling angles less than 10° when the radius is lower than the capillary constant of $R_c = 2.7$ mm [48,52]. Water droplets are prevented from wetting the rough structures; meanwhile, air is confined between the physical structures to form an air layer, thereby retaining the droplets in a Cassie state and maintaining their spherical shape. In recent years, researchers reported another type of superhydrophobic surface; i.e., lubricant surfaces, which are also referred to lubricant-infused surfaces (LIS) or slippery liquid-infused porous surfaces [53,54]. On such surfaces, low-surface-energy and low-vapor-pressure lubricants are stabilized with porous or nanostructured textures via capillary forces, forming interfaces that are chemically homogeneous and atomically smooth [55]. Unlike superhydrophobic surfaces exhibiting Cassie wetting states, lubricant surfaces use a low surface energy lubricant to fill the voids of structured solid substrates, separating the immiscible liquid and solid substrate, and shifting the solid-liquid contact to a liquid-liquid contact. For more in-depth information on the contact angles and wetting principles of superhydrophobic and lubricant surfaces, refer to the recent reviews by Drelich J.W. et al. and Peppou-Chapman, S. et al. [56,57].

Liquid evaporation occurs naturally when the liquid vapor in the surrounding atmosphere is not saturated. The evaporation process is considered a diffusion-controlled process, although it is complex and can be described by simultaneous mass and heat transfer equations involving diffusion and convection [58]. Droplet evaporation has become a research hotspot in recent years because of its crucial role in mass and heat transfer [59–61].

Free-droplet evaporation is an ideal system to study droplet evaporation. In this system, the droplet is perfectly spherical without contacting the solid substrate, and its evaporation process is the same across the entire spherical surface; this is known as isotropic (radially symmetric) evaporation. The evaporation is influenced only by the diffusion of liquid molecules into the surrounding air, and the change in droplet volume with time follows [62,63]:

$$V^{2/3} = V_0^{2/3} - \Lambda t \tag{1}$$

where V_0, Λ, and t represent the initial volume of the droplet, rate of surface reduction, and evaporation time, respectively. For a free droplet, the volume (V) is related to the radius R as $V = \frac{4\pi R^3}{3}$.

Considering the time derivative of Eq. (1), we obtained the initial evaporation velocity of the droplet (v_{ev}) as:

$$v_{ev} = \frac{1}{2}\left(\frac{3}{4\pi}\right)^{2/3}\frac{\Lambda}{R_0} \tag{2}$$

where v_{ev} and R_0 represent the speed of the receding droplet-air interface and initial droplet radius.

For an ideal free, spherical droplet Λ can be determined analytically [62,64] as:

$$\Lambda_{free} = 2\left(\frac{4\pi}{3}\right)^{2/3}\frac{D_{air} m \Delta P}{\rho k_B T} \tag{3}$$

where, D_{air}, m, ρ, ΔP, and k_BT represent diffusion coefficient of vapor molecules in the air, mass of a vapor/liquid molecule, density of the liquid, pressure difference between the droplet surface and outer vapor layer, and thermal energy of the system, respectively.

Free droplets represent an ideal state; however, in practical applications and manufacturing processes, droplets come into contact with substrates under various conditions, making it more meaningful to clarify the evaporation process of droplets on solid substrates [2–20]. Unlike droplets on superhydrophilic, hydrophilic, or hydrophobic surfaces, which exhibit fully or partially wetted cap-shaped configurations, droplets on super-liquid-repellent surfaces exhibit nearly perfect spherical shapes, closely resembling the state of free droplets. In recent years, researchers have gained a deeper understanding of droplet evaporation on superhydrophobic surfaces owing to the development of superhydrophobic surface fabrication techniques and research on liquid wetting processes [65–68]. Droplet evaporation on superhydrophobic surfaces is divided into constant contact angle (CCA) and constant contact radius (CCR) modes [67,69,70]. Droplets in the Cassie state adopt the CCA mode because the contact line remains free to move during evaporation, maintaining a CCA whereas the contact radius gradually decreases (Fig. 1a). Conversely, droplets in the Wenzel state are more likely to exhibit the CCR mode as the contact line being strongly pinned, resulting in a gradual decrease in the solid surface contact angle while the contact radius remains nearly constant (Fig. 1b). The specific evaporation mode adopted depends on factors such as the actual surface structure and droplet properties. For superhydrophobic surfaces composed of microscale (several to tens of micrometers and above) patterned structures, droplets are pinned on the microstructured surface, resulting in CCR evaporation. After the droplet shrinks to a certain extent, the contact line jumps from the microstructure to the inner structure and transitions to CCA evaporation. These two evaporation modes alternate in cases where the droplet does not wet the structural gaps (Fig. 1c) [71]. Once liquid wetting occurs, the Cassie state transitions to the Wenzel state, which changes to the CCR mode; this is more likely to occur with an increase in the spacing between structures because it causes the droplet volume to decrease to a point where it transitions to the wetting state (Fig. 1d) [72]. For superhydrophobic surfaces composed of nano- or sub-micrometer-scale structures, droplets are less likely to transition from the Cassie state to the Wenzel state, and therefore, they initially undergo CCA mode evaporation. When the droplet is sufficiently small, it transitions to the CCR mode or CCA/CCR alternating mode [70,73–77]. However, gravity-induced deformation occurs when the initial liquid volume is large, causing the droplet to undergo CCR mode evaporation, which then transitions to the CCA mode once the droplet returns to a spherical shape [78]. Although droplets on superhydrophobic surfaces can exhibit different evaporation modes, the surface area of the droplet decreases linearly with evaporation time in both modes, thereby providing a description of the evaporation process based on the change in the droplet surface area [63,78].

Although the small contact area between the droplet and superhydrophobic surface causes the droplet to present an almost perfect spherical shape, the effect of the presence of the supporting surface on the diffusion of molecules into the environment is undeniable. Therefore, it is necessary to consider the wetting behavior (contact angle) of the surface and its effect on droplet evaporation. Based on this, Picknett and Bexon corrected the evaporation rate of droplets with spherical cap shapes by integrating the effect of the contact angle on the evaporation rate [64].

$$V^{2/3} = V_0^{2/3} - \Lambda_{sessile} t = V_0^{2/3} - \frac{4\pi D_{air} m}{3\rho} \frac{f}{\beta} \Delta P \bullet t \tag{4}$$

with $\beta = (1 - cos\theta)^2(2 + cos\theta)$ as the contact angle θ, and $f = 0.00008957 + 0.633\theta + 0.116\theta^2 - 0.08878\theta^3 + 0.01033\theta^4$ for θ(rad) above 10°.

Thus, the surface reduction rate of the droplet can be calculated as:

$$\Lambda_{sessile} = \left(\frac{8\pi}{3}\right)^{2/3} \frac{D_{air} m \Delta P}{\rho k_B T} \frac{f}{\beta^{1/3}} \tag{5}$$

For water droplets, the pressure difference ΔP in Eq. (5) can be expressed in terms of relative humidity (RH) as $\Delta P = (1 - RH)P_0$, where P_0 presents the saturation vapor pressure. Our previous study revealed a linear decrease in $V^{2/3}$ for pure water droplets on super-liquid-repellent surfaces [79].

Compared to the superhydrophobic surface, the contact area between the droplet and the lubricant surface increased because the lubricant-impregnated hydrophobic surface covered the physical structure. Further, the capillary force drives the lubricant to climb upward along the bottom of the droplet to form a wetting ridge. Based on the amount of lubricant and choice of droplet, the wetting ridge can expand further, enveloping the entire droplet and forming a cloaking layer (Fig. 1e,f) [57].

The differences in the surface energies of oil, water, and air can be expressed by the spreading coefficient $S_{LO} = \gamma_{LA} - \gamma_{LO} - \gamma_{OA}$. When S_{LO} was positive, oil wrapped around the water droplet, minimizing its surface energy. When $S_{LO} < 0$, the main part of the droplet was still covered by oil [80–82]. The top of the droplet was exposed and surrounded by an oil ridge, and a distinct liquid-liquid-air contact line was observed (Fig. 1f) [38]. Therefore, the droplets on the lubricant surfaces exhibited a semi-spherical shape with a significantly reduced apparent contact angle. However, the presence of a lubricant layer dramatically

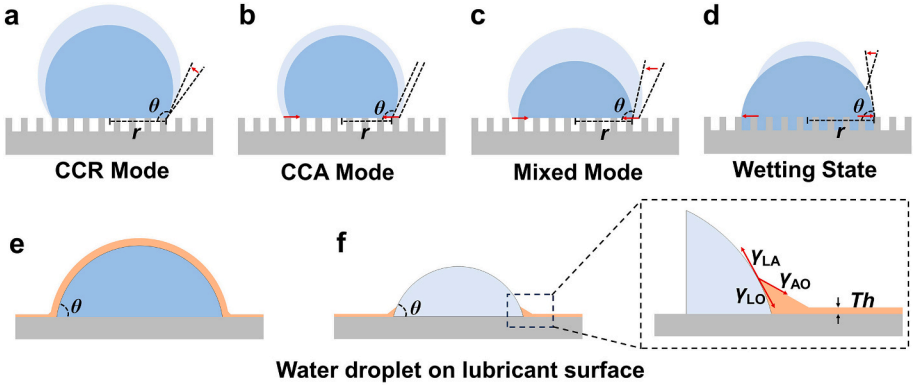

Fig. 1. Typical evaporation modes of water droplets on super liquid-repellent surfaces. (a-d) Water droplet evaporation on superhydrophobic surface in constant contact radius (CCR) (a), constant contact angle (CCA) (b), mixed (c), and (d) the droplet evaporation in Wenzel wetting mode, respectively. Reproduced with permission [77]. Copyright 2013, American Chemical Society. (e-f) The evaporation on lubricant surfaces with the formation of a cloaking layer (e) or a wetting ridge (f) by the lubricant.

reduced the friction between the droplet and surface, which allowed the droplet to detach freely at a slight inclination angle [83,84]. The lubricant layer separated the droplets on the lubricant surfaces instead of directly contacting the substrates, preventing the contact line from pinning. The viscous dissipation of the liquid drives movement and evaporation [57]. Droplet evaporation on lubricant surfaces exhibited a more complex mixed mode. Initially, droplet evaporation followed the CCR mode, and subsequently evaporation occurred exclusively in the CCA mode. The driving force $F = \gamma_{LA}(cos\theta_d - cos\theta_e)$ becomes sufficient to overcome the energy barriers with a decrease in the contact angle. Here, γ_{LA}, θ_d, and θ_e represent the interfacial tension between the droplet and vapor, dynamic contact angle, and equilibrium contact angle, respectively. In the final stage, the contact angle decreases with a decrease in the contact diameter until the droplet disappears [84]. In addition, evaporation was concentrated at the uncovered top of the droplet because most droplet surface was covered by a lubricant. An internal liquid flow towards the air-droplet interface occurs inside the droplet as th evaporation proceeds, thereby resulting in anisotropic evaporation (non-radially symmetrical evaporation). The evaporation is slow on lubricant surfaces because the impregnant lubricant reduces the evaporative area. Droplets on lubricant surfaces have significant aspect ratios and low heat dissipation rates, which extend the thermal resistance path [38,85].

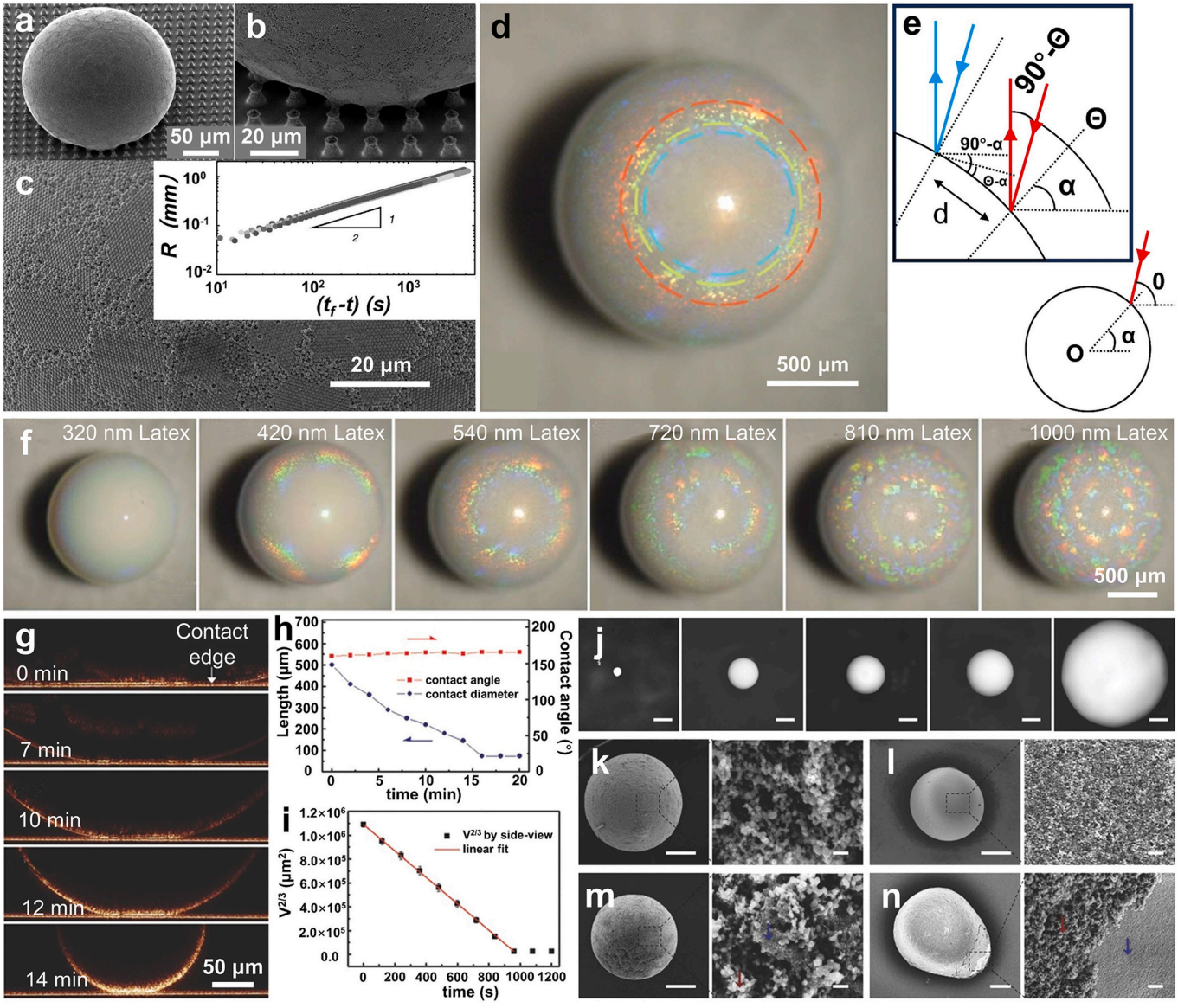

Fig. 2. Supraparticle fabrication on superhydrophobic surfaces. SEM images of the supraparticle in contact with a microcolumn array (a), contact area (b), and crystalline patches of the supraparticle surface (c). The inset of (c) presents the radius against $t_f - t$ [28]. (d) Optical image of a 540 nm latex opal supraparticle. (e) Schematics of angles for calculating the theoretical wavelength for a particular color ring. (f) Optical microscopy images of opal supraparticles with different sizes of primary particles. Reproduced with permission [29]. Copyright 2008, Wiley-VCH. (g) Drop evaporation imaged by confocal microscopy. (h) Contact diameter and contact angle, and (i) $V^{2/3}$ variations with time. (j) Optical images of mesoporous TiO_2 supraparticles with diameters of 50, 160, 200, 250, and 550 μm, scale bars are 100 μm. (k–n) SEM images of mesoporous supraparticles fabricated by (k) TiO_2, (l) SnO_2, (m) TiO_2/SnO_2 mixture, and (n) $SnO_2@TiO_2$ core-shell particle. The scale bars in all images on the left are 50 μm, and on the right are 100 nm (except the right image of (n) is 1 μm). The blue and red arrows indicate SnO_2 and TiO_2, respectively. Reproduced with permission [88]. Copyright 2015, Wiley-VCH. (For interpretation of the references to color in this figure legend, the reader is referred to the web version of this article.)

3. Structural regulation of supraparticles fabricated on surfaces

3.1. Supraparticle fabrication mediated by droplet evaporation on superhydrophobic surfaces

Superhydrophobic surfaces have unique advantages in the preparation of spherical supraparticles. For example, water droplets on such surfaces exhibit almost spherical shapes, ultra-small contact areas, and minimal friction along the three-phase contact line. The droplets act as templates to drive the aggregation and assembly of the dispersed colloidal particles, forming spherical supraparticles after evaporation [27,35]. Marin et al. explored the formation of spherical supraparticles by investigating the evaporation of polystyrene (PS) particle dispersion droplets on microcolumn array-based superhydrophobic surfaces (Fig. 2a) [28]. The constructed hanging microcolumn structure prevented the wetting state transition, avoiding the three-phase contact line from being pinned. Therefore, dispersion droplets maintained the Cassie-Baxter state, forming spherical supraparticles with colloidal crystalline patches on the surface (Fig. 2b, c).

When a droplet evaporates at a CCA, the change in radius change is given by

$$R(t) \sim \left[D'\left(t_f - t\right)\right]^{1/2} \tag{6}$$

In Eq. (6), R represents the droplet radius, $D' = D_{air}\Delta P/\rho$, where D_{air}, ΔP, t_f, and t represent the diffusion constant for vapor in air [86,87], vapor concentration difference between the drop surface and surrounding environment, total time for complete evaporation, and actual time, respectively.

The droplet radius reaches its minimum value r_{SP} (radius of the supraparticle) as colloidal particles are present and the internal particles are densely packed ($\hat{t} = t_f - r_{SP}^2/D'$). The inset in Fig. 2c shows the relationship between the radii of the colloidal dispersion droplets and $t_f - t$, where the presence of colloidal particles inside the droplet does not affect the evaporation process. During evaporation, the gas-liquid interface moves inward at a rate of $dR/dt \sim D'/R$. The interface shrinkage rate sharply increased with a decrease in droplet volume, until it reached the shrinkage limit r_{SP}.

The size of the supraparticles depends on the number of particles inside the droplet when an assembled structure is formed by the colloidal particles. The size of supraparticles r_{SP}/r_p can be adjusted in the range of 100–1000 (where r_p represents the radius of the primary particle) by controlling the initial concentration or volume of doplets. In addition, the size of the supraparticles depends on the packing fraction of the primary particles. The global packing fraction is given by:

$$\Phi \equiv N\left(\frac{r_p}{r_{SP}}\right)^3 \tag{7}$$

where N represents the total number of primary particles in the droplet.

Unlike the well-known relationship $r_{SP}/r_p \backsim N^{1/3}$, the packing fraction deviates from one-third scaling, especially when the number of particles is small. An increase in the number of monodisperse spherical particles causes an ordered close packed structure to form inside the supraparticle with a packing fraction approaching a perfect hexagonal with $\Phi = 0.74$. Conversely, the packing fraction of the supraparticle decreases with a reduction in the number of monodisperse spherical particles, which is even lower than the random close packing (RCP) limit of $\Phi = 0.64$, thereby resulting in a supraparticle with disordered particle arrangement and some internal defects.

The motion and assembly of particles confined within spherical droplets are influenced by particle diffusion and convective transport induced by the shrinkage of the gas-liquid interface. Therefore, the critical number of particles N_c required for the transition from an ordered to a disordered assembly of supraparticles can be estimated by comparing the diffusion-driven assembly and convective transport timescales. The particles can be arranged in an ordered packing crystal phase when the diffusion time of the primary particles across the droplet radius is less than the hydrodynamic time scale. The diffusion time for the particles to move to their appropriate positions in the crystalline phase is $t_d = r_p^2/D_p$, where D_p represents the diffusion coefficient of the particles in the liquid. The hydrodynamic time scale $t_h = L/|dr/dt|$, where $r_{(t)}$ represents the droplet radius, and L represents the distance between particles, which primarily depends on the concentration of particles in dilute solutions ($L \gg r_p$), $L = N^{-1/3}r$.

The ratio of both timescales is given by:

$$\mathscr{A}(t) \equiv \frac{t_d}{t_h} = \left|\frac{dr(t)}{dt}\right| \frac{t_d}{L} = \frac{D'}{D_p} N^{1/3} \left(\frac{r_p}{r(t)}\right)^2 \tag{8}$$

During evaporation, $\mathscr{A}(t)$ increases with a decrease in the droplet radius until the limit $r = r_{SP}$ is reached. A crossover between the timescales is obtained when hydrodynamic time is equal to the diffusion time, i.e., $\mathscr{A}(t) = 1$. If the cross-over is achieved when $r \gg r_{SP}$, the amount of crystalline clusters is still very small. From this time point, the shrinkage rate of the interface was too high, and the primary particles did not have sufficient time to crystallize, resulting in a relatively low packing fraction. If the cross-over is obtained when $r \ll r_{SP}$, the particle packing has already been ordered, which results in a high packing fraction. During droplet evaporation, the trend of the decreasing droplet radius attributed to solvent evaporation was the same. Therefore, the time required to achieve a dense packing of particles depends entirely on the number of particles. If N is large ($N > N_c$), the cross-over of timescales will occur relatively early, i.e., well before $\mathscr{A} = 1$, thereby allowing for the formation of ordered particle packing inside the supraparticle. According to $r_{SP}/r_p \sim N^{1/3}$ and $\mathscr{A} = 1$, the critical number of particles above which ordered supraparticles are obtained can be calculated using Eq. (9):

$$N_c \sim \left(\frac{D'}{D_p}\right)^3 \tag{9}$$

The time-dependent packing fraction for monodisperse spherical particles that can easily assemble into ordered structures is defined as $N\left(r_p/r(t)\right)^3$. As the droplet evaporates, the packing fraction increases until it reaches the final value Φ. At cross-over ($\mathscr{A} = 1$), the packing fraction of the droplet is denoted as Φ^*. A small Φ^* indicates a small amount of crystalline clusters. Further, when Φ^* is large, crystalline clusters have already formed. After the cross-over point, the shrinking speed of the interface is too fast to provide sufficient time for promoting ordering, which leads to the compression of the ordered particle clusters. Droplets with a large Φ^* have a large Φ. A packing fraction larger than the random close packing (RCP) limit can be achieved when $\Phi^* \gtrapprox 0.1$.

Although ordered crystalline structures can be formed in the supraparticles, the assembly process is not sufficiently long to prevent point and line defects. This resulted in the formation of ordered crystalline patches on the supraparticle surfaces; the size of these patches is related to the size of the supraparticles. Larger supraparticles with reduced surface curvatures form larger crystalline patches, and their radial curvatures do not exceed the size of the primary particles. The relationship between the size S of the patches and the supraparticle radius r_{SP} and particle size r_p is $S/r_{SP} = arccos\left(1 - r_p/r_{SP}\right)$. For supraparticles with $r_{SP} = 50$ μm and $r_p = 0.5$ μm, the typical size of crystalline patches on the surface is ~15 μm, which is consistent with the order of magnitude characterized by SEM (Fig. 2c). Therefore, the sizes of the crystalline patches on the supraparticle surface can be predicted.

Periodicity at the micrometer and sub-micrometer length scales endows colloidal assembly structures with light-manipulation capabilities similar to those of natural opals. Properties such as long-range ordering, maximum packing density, well-defined pore sizes, and high surface-to-volume ratios render the assembled materials useful in photonics,

optical diffraction, antireflective coatings, and anisotropic particle manufacturing. Rastogi et al. realized the green and controllable fabrication of spherical opal-like supraparticles by evaporating monodisperse PS dispersion droplets on low-density polyethylene superhydrophobic surfaces [29].

As the solvent evaporates, the free volume of the colloidal particles within the droplet gradually decreases, slowly confining the thermal motion of the primary particles and driving them to assemble into densely packed crystals. An increase in particle concentration results in colloidal crystals that reflect light at specific wavelengths. After 15 min of evaporation, the droplet surface exhibits colored ring-like diffraction patterns (Fig. 2d). Approximately 60 min later, all of the solvent evaporated, forming supraparticles assembled from PS spheres arranged in a hexagonal close-packed crystal arrangement.

Supraparticles assembled from highly ordered particles sparkle in a multitude of colors. The colored regions are organized in concentric rings (Fig. 2d). The surface of the opal-like supraparticles includes localized crystal regions, with each region diffracting light in a specific direction relative to a fixed light source and the orientation of the crystal plane, thereby causing fragmented rings in areas with slightly different colors. Unlike typical photonic crystals, the phenomena of diffraction and reflection of light occur only on the surface of supraparticles because of their curved surfaces. The difference in the optical paths of the light waves reflected by two adjacent grooves (particle lines) on the surface results in constructive or destructive interference, thereby inducing colored ring patterns. The formula for the path difference on the curved surface of the supraparticles is [89] (Fig. 2e):

$$n\lambda = d \times [sin(90-\alpha) + sin(\theta-\alpha)] \tag{10}$$

where $n = 1, 2, 3 \ldots$ represents the first, second, third, sets of rings, respectively. Further, λ, θ, α and d represent the wavelength of a specific spot on the colored ring, angle between the incident beam and horizontal plane, angle between the radial direction of the examined colored spot and horizontal plane, and interplanar spacing of the colloidal crystal, respectively. The primary particles were arranged in a face-centered cubic lattice for ordered colloidal crystals, with the (111) plane parallel to the outer interface. The interplanar spacing of the (111) plane is $d = \sqrt{2/3}D$, where D represents the diameter of the colloidal particles. The space between the particles on the surface of the supraparticles can be adjusted by regulating the size of the PS microspheres, thereby altering the colored ring patterns. Consequently, the supraparticles formed from the particles of the same size exhibited the same ring patterns. In contrast, the size and number of colored ring patterns formed by differently-sized particles varied significantly (Fig. 2f).

Wooh et al. constructed a series of supraparticles through droplet evaporation on superamphiphobic surfaces using non-spherical or non-monodisperse nanoparticles as building blocks [88]. Superamphiphobic surfaces repel water and non-polar liquids, further expanding the range of liquid species and broadening the systems for preparing supraparticles via droplet evaporation. A superamphiphobic surface was achieved by constructing a porous silica substrate using candle-soot as a template, followed by treatment with 1H, 1H, 2H, 2H-perfluorooctyltriethoxysilane for hydrophobization. The porous silica structure entraps tiny air pockets, preventing the liquid from wetting the structure. The droplet sits on top of the protrusions, maintaining a spherical shape owing to the interfacial tension of the liquid, with a receding contact angle of ~163°. Owing to the microstructure of the substrate, 1 μL of an aqueous dispersion of TiO_2 nanoparticles (0.1 vol% TiO_2 nanoparticles, diameter 21 nm, P25 Degussa Evonik) maintains a spherical shape (Fig. 2g). Further, the contact diameter decreases continuously as evaporation proceeds, the contact angle θ remains above 160° (Fig. 2h), $V^{2/3}$ decreases linearly with time (Fig. 2i), and dispersed nanoparticle droplet gradually transforms into solid particles.

During evaporation, TiO_2 nanoparticles assembled through capillary pressure. The maximum capillary pressure during drying is $\Delta P \approx 10\gamma/r$ for nanoparticles with a radius r that can be completely wetted, where γ represents the surface tension of the liquid [90,91]. At $r = 12$ nm, the pressure was ~60 MPa which is sufficient to bring the nanoparticles into direct contact, while the van der Waals forces further increase cohesion. Therefore, the prepared mesoporous supraparticles were highly stable and remained in the solvent for several months without disassembling into nanoparticles, thereby making them suitable for application in powder and dispersion forms. The initial volume and concentration of the dispersion droplets can be employed to control the size of the mesoporous supraparticles ranging from micrometers to submillimeter, with the porosity determined to be 53 % ± 1 % (Fig. 2j). The proposed method exhibits high flexibility because different mesoporous supraparticles can be prepared by changing the primary particles (Fig. 2k,l). Mixing different materials such as TiO_2/SnO_2, TiO_2/ZnO, and $TiO_2/Fe_2O_3@SiO_2$ enables the fabrication of multi-component supraparticles (Fig. 2m, n). Rapid and automatic particle production was achieved using a multi-nanodroplet dispenser (Nano-Plotter, Gesim, Germany) to address the issue of relatively long evaporation times. A nano-plotter with a piezoelectric nanotip can dispense droplets with a repeatable volume at frequencies up to 1 kHz, which enables the controlled preparation of a large number of droplets in a short time. Such small TiO_2 nanoparticle dispersion droplets (~0.7 nL) can completely dry within seconds, forming monodisperse mesoporous TiO_2 supraparticles (diameter: ~10 μm) and achieving a prototype of a high throughput supraparticle fabrication.

In addition to the droplet templating action driving the primary particle assembly into spherical supraparticles, various factors such as particle interactions [30,92,93], particle components [29,79,92,94], and external fields [32,92,95] significantly affects the assembly behavior of the constituent particles or the morphology of the supraparticles [96–102].

3.1.1. Interactions between the building blocks

Interactions between particles directly affect their motion, which determines the morphology and structure of the supraparticles. The interaction forces of particles in evaporating media include van der Waals (F_{vdw}), electrostatic (F_{el}), capillary (F_{cap}), hydrodynamic forces (F_H), and etc. [103,104]. The total interaction force $F_{total}(d)$ between two microspheres with radius r and surface separation d can be expressed as

$$F_{total}(d) = F_{vdw} + F_{el} + F_{cap} + F_H + \cdots\cdots \tag{11}$$

The van der Waals force is given by [105].

$$F_{vdw} = -\frac{A_H r}{12d^2} \tag{12}$$

where A_H is the Hamaker constant [106].

The electrostatic force can be expressed as [107,108].

$$F_{el} = \frac{2\pi\varepsilon\varepsilon_0 r\psi^2}{\lambda_D} e^{-\frac{d}{\lambda_D}}\left[1 - e^{-\frac{d}{\lambda_D}}\right] \tag{13}$$

where ψ represents the surface potential. Further, λ_D represents the Debye length and is given by

$$\lambda_D = \sqrt{\frac{\varepsilon\varepsilon_0 k_B T}{2 \bullet 10^3 N_A e^2 I}} \tag{14}$$

where, k_B, T, e, N_A, and I represent the Boltzmann constant, temperature, elementary charge, Avogadro's number, and molar ionic strength of the electrolyte, respectively.

$$I = \frac{1}{2}\sum_{i=1}^{n} c_i z_i^2 \tag{15}$$

where coefficient $\frac{1}{2}$ accounts for the inclusion of both cations and anions in the electrolyte solution, c_i represents the molar concentration of ion i

in mol/L, z_i represents the charge number of the ion, and I represents the sum of all ions in the solution. The ionic strength is equivalent to the concentration of a 1:1 type of electrolyte, sodium chloride (NaCl), where each ion is singly charged.

The capillary force between two spherical particles with the same size is related to the contact angle on the particle surface (θ) and the surface tension of the solvent (γ) [109].

$$F_{cap} = 2\pi\gamma r cos\theta \tag{16}$$

The hydrodynamic force is given by [110,111].

$$F_H = -\frac{3\pi\eta v r^2}{2d} \tag{17}$$

where, η represents the dynamic viscosity, and v represents the velocity of a particle moving towards another one.

Thus, the total interaction between the two particles in the evaporating medium can be expressed as

$$F_{total}(d) = -\frac{A_H r}{12d^2} + \frac{2\pi\varepsilon\varepsilon_0 r\psi^2}{\lambda_D} e^{-\frac{d}{\lambda_D}}\left[1 - e^{-\frac{d}{\lambda_D}}\right] + 2\pi\gamma r cos\theta - \frac{3\pi\eta v r^2}{2d} + \cdots\cdots \tag{18}$$

The capillary force plays a significant role only in the range of a few nanometers, whereas hydrodynamic forces are quite complex to evaluate; therefore, a commonly used Derjaguin-Landau-Verway-Overbeek (DLVO) theory was developed to describe the interactions for charged colloidal particles. The DLVO theory mainly considers the interaction results from electrostatic repulsion and van der Waals attraction for a limited interparticle distance by neglecting external physical forces, capillary forces, hydrodynamic forces, etc. The corresponding force between two spheres of radius r is:

$$F(d) = \frac{2\pi\varepsilon\varepsilon_0 r\psi^2}{\lambda_D} e^{-\frac{d}{\lambda_D}}\left[1 - e^{-\frac{d}{\lambda_D}}\right] - \frac{A_H r}{12d^2} \tag{19}$$

The presence of charged ions in the dispersion shields the surface charge of the colloidal particles, which is reflected as a change in the Debye length. Therefore, the interactions between colloidal particles can be regulated by modulating the ionic strength of the dispersion solution. We explored the drying process of colloidal PS particle dispersions and the effect of interparticle interactions on the morphology and structure of supraparticles at different salt concentrations [93]. Water droplets containing monodisperse colloidal PS particles exhibited radially symmetric evaporation on superhydrophobic surfaces, forming spherical core-shell supraparticles with highly ordered surfaces and disordered interiors (Fig. 3a-d) because monodisperse PS colloidal particles have negative charges, and electrostatic repulsion dominates the interaction between colloidal particles. With liquid droplet evaporation, the shrinkage of the gas-liquid interface drives the colloidal particles closer to each other. However, electrostatic repulsion prevents particle

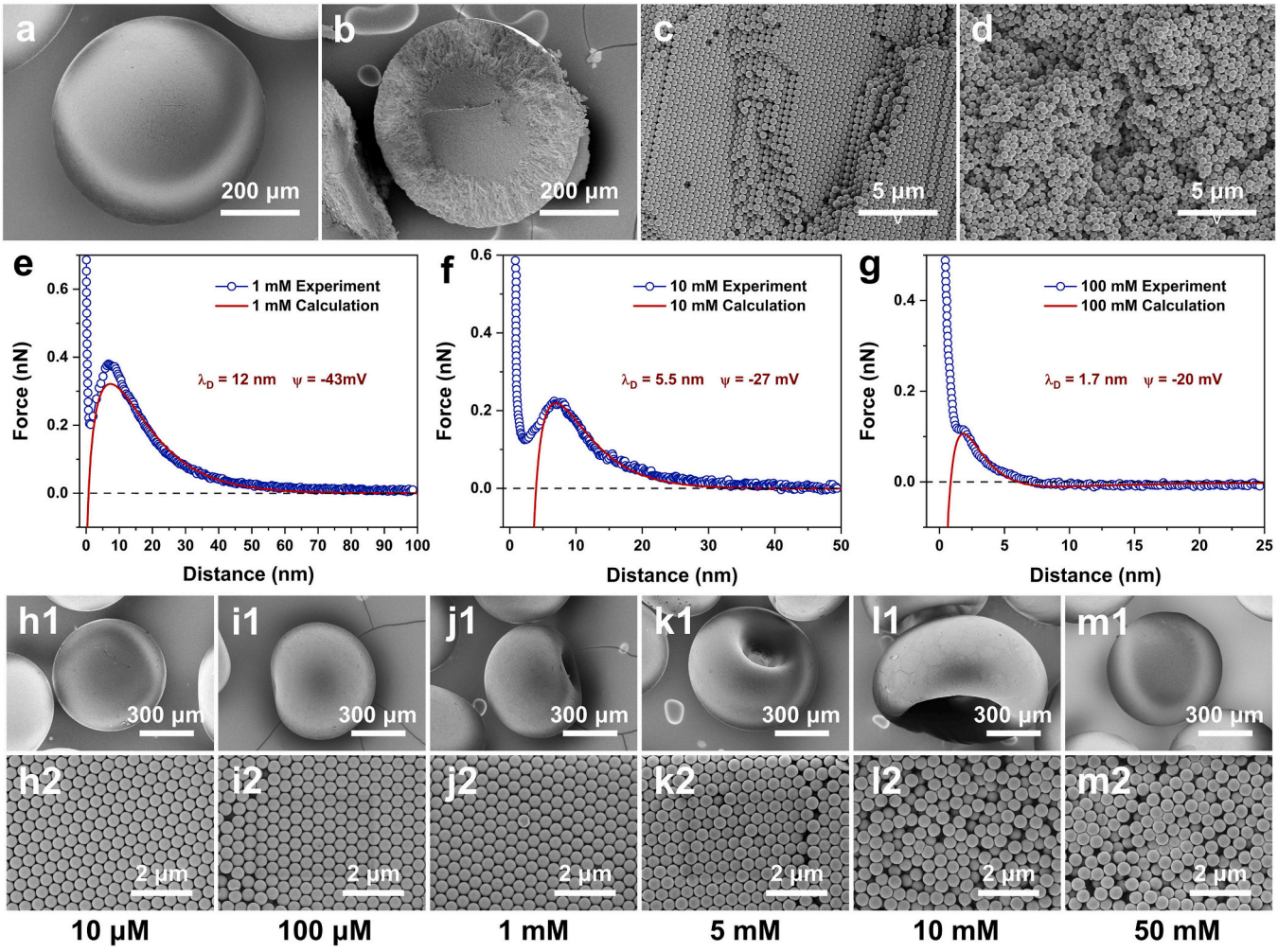

Fig. 3. Controlling supraparticle shape and structure by tuning colloidal interactions. SEM images of the spherical supraparticle (a), cross-sectional (b), crystalline shell (c), and the random core (d). (e-g) Single colloid interaction forces at different NaCl concentrations (1, 10, and 100 mM, respectively). (h) Shape (1), surface structure (2), and cross-section (3) of supraparticles obtained by evaporating suspension droplets with NaCl concentrations of 10 μM, 100 μM, 1 mM, 5 mM, 10 mM, and 50 mM. Reproduced under terms of the CC-BY license [93]. Copyright 2022, The Authors, published by Elsevier.

contact, forming an orderly assembled structure and enhancing the packing fraction until the liquid evaporates completely. Finally, the evaporation of the liquid drives the particles to approach each other at a distance of a few nanometers, whereas the capillary force dominates and makes the particles contact each other. Then, the repulsive force is transformed into a strong van der Waals attraction, which ultimately leads to the formation of a stable structure.

The introduction of NaCl into the dispersion resulted in the electrostatic shielding of the colloidal particles. The Debye length decreases from ~12 nm (Fig. 3e) to ~5.5 nm (Fig. 3f) and 1.7 nm (Fig. 3g) with an initial increase in the NaCl concentration from 10 μM to 10 mM, and then to 100 mM, respectively. Meanwhile, the surface potential decreases from more than −50 mV to −20 mV. Consequently, the potential barrier decreases significantly with an increase in the salt concentration and approaches zero. Further, when the salt concentration exceeds a critical value, the repulsive barrier is no longer high enough to counter the van der Waals interactions, which leads to an irreversible adhesion of the colloidal particles and the formation of agglomerated structures.

In the presence of NaCl, the average distance between the colloidal particles in the shell is small because of the screening by the electric double layer. Consequently, the transition from dynamic colloidal crystals to solid shell structures occurred earlier, inducing a reduction in the crystalline shell thickness with increasing NaCl concentration (Fig. 3h). After the shell solidified, a significant volume remained in the center. As the water evaporated, capillary forces were generated between the colloidal particles on the surface of the evaporating droplet. This pressure difference caused the buckling of the outer shell (Fig. 3h). The solidified shell suppressed the advective motion of the colloidal particles, leading to a lack of driving force for densification and the subsequent crystal formation. Thus, the interior structure remained amorphous. At extremely high salt concentrations of 50 and 100 mM, the electrostatic repulsion was no longer strong enough to stabilize the colloidal dispersion. The colloidal particles agglomerate in the solution before evaporation, thereby overcoming the buckling caused by capillary forces, and instead forming disordered, porous, and spherical supraparticles. These results demonstrate the critical role of colloidal particle interactions in controlling droplet evaporation, supraparticle morphology, and supraparticle structure. This study provides a theoretical basis for the construction of supraparticles with specific structures and functions.

Sperling et al. added NaCl to fumed silica (FS) dispersion droplets and evaporated them on a superhydrophobic surface, resulting in supraparticles with an anisotropic morphology [30]. The addition of electrolytes effectively changed the repulsive force between the silica nanoparticles, promoting the assembly of the building blocks into aggregated structures. Consequently, the silica nanoparticles accumulated at the gas-liquid interface as evaporation proceeded and formed a rigid shell structure, delaying the shrinkage of the contact line. The capillary force generated by the liquid evaporation drives the shell structure to bend inward, disrupting the symmetry of the supraparticles (Fig. 4a). This effect was less pronounced at low NaCl concentrations, which allowed the droplets to maintain isotropic evaporation, thereby resulting in spherical and doughnut-shaped supraparticles (Fig. 4b). Salt concentrations above 5 mM caused the evaporating droplets to deform at a certain point, elongate their shape until the end of evaporation, and form anisotropic boat-shaped structures (Fig. 4b). These results confirm the effect of the electrolyte-induced electrostatic double-layer forces on the formation of supraparticles during evaporation.

In addition to the ion strength, Sekido et al. utilized the pH of the dispersion to regulate the assembly of supraparticles composed of colloidal particles modified with responsive polymers [112]. Poly[2-(diethylamino)ethyl methacrylate] (PDEA), a pH-responsive polymer, was shown to be hydrophilic and hydrophobic at low and high pH, respectively. Therefore, PDEA-modified PS particles were uniformly dispersed at pH 3 and aggregated at pH 10 because of the deprotonation of the polymer (Fig. 4c). Uniformly dispersed colloidal droplets underwent radial symmetric evaporation on superhydrophobic surfaces, and the capillary force generated by the evaporation drove the colloidal particles to assemble in an ordered manner to form dense supraparticles with a packing fraction of 72 % (Fig. 4d,e). In contrast, at pH 10, the colloidal particles aggregated in the dispersion as the pH-responsive PDEA changed from hydrophilic to hydrophobic. The capillary force only compresses the aggregate structure instead of driving individual colloidal particles to rearrange and assemble into densely packed structures. This results in supraparticles with disordered assemblies and a particle packing fraction of only 56 % (Fig. 4f,g). The density of the assembly structure directly affects the properties of the supraparticles. At pH 3, the supraparticles exhibited a low porosity and high elastic modulus of ~27 % and ~ 62 MPa, respectively. In contrast, the porosity of the supraparticles reached 44 % with a modulus of ~39 MPa at pH 10.

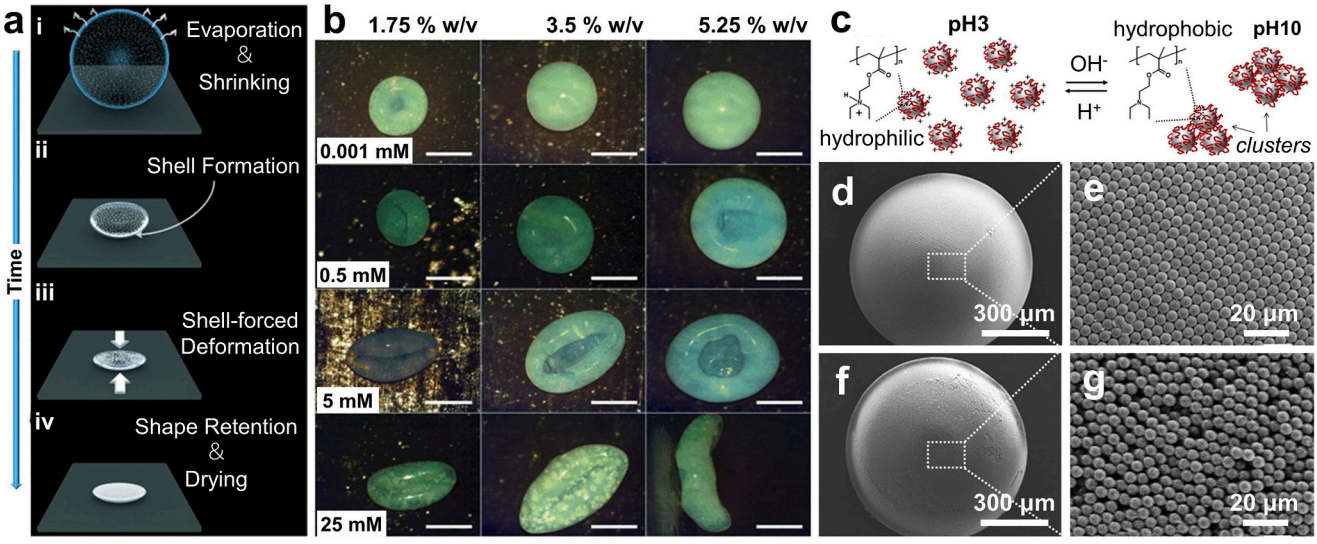

Fig. 4. Ionic-strength-controlled supraparticle shape regulation. (a) Schematic of the mechanism of supraparticle elongation during evaporation. (b) Examples of different types of supraparticles formed after the completion of the drying process as a function of FS and electrolyte concentrations, scale bars: 0.5 mm. Reproduced with permission [30]. Copyright 2014, Wiley-VCH. PH-responsive particle mediated supraparticle structure controlling. (c) Scheme of the pH-responsive dispersion/aggregation behavior of Poly[d-(diethylamino)ethyl methacrylate] (PDEA)–PS particles. SEM images of supraparticles fabricated using pH 3 (d, e) and 10 (f, g) dispersions (1 μL). Reproduced with permission [112]. Copyright 2017, American Chemical Society.

Thus, controlling the degree of particle dispersion provides an effective strategy for constructing supraparticles with different structures and mechanical properties.

3.1.2. Components

The components of the droplet used for evaporation are essential factors for controlling the structure and properties of the supraparticles. Relevant research was conducted in our previous studies [79,94]. Porosity, a critical parameter for supraparticles, dramatically affects their performance in practical applications, such as heterogeneous catalysis, adsorber materials, and drug carriers. For many applications, supraparticles with high porosity are required to facilitate the diffusion of analytes or reactants. Based on organic-inorganic hybridization, we achieved the controllable tuning of the porosity of the supraparticles by utilizing a heterogeneous structure constructed by the evaporation of the droplets on superamphiphobic surfaces [94]. Fig. 5a shows droplets containing TiO_2 and PS nanoparticles evaporated on a superamphiphobic surface to prepare spherical binary supraparticles with uniformly distributed two-phase materials (Fig. 5b,c). PS undergoes degradation at 330–400 °C, and therefore, the calcination of the binary supraparticles at 500 °C can completely remove the polymer phase, thereby forming highly porous supraparticles derived from the PS templates (Fig. 5d,e). During the assembly process, TiO_2 nanoparticles were attracted to each other to form a porous stacking structure with a porosity of ~66 %. The introduction of polymer particles, in addition to acting as templates, creates interconnected pore structures because of the contact between the polymer particles, thereby increasing the porosity of the supraparticles. The use of PS microparticles of different sizes can regulate the size of the macropore structure from hundreds of nanometers to micrometers. Changing the ratio between inorganic and organic particles allows for proportional variation between large macropores and interconnected pore spaces. The obtained maximum porosity reached 92.1 %, which significantly improved the catalytic performance of the TiO_2 supraparticles. Although solid particles in the obtained supraparticles accounted for less than 10 % of the volume, the calcination process facilitated the fusion of TiO_2 nanoparticles because of the slight crystalline phase transitions, which ensured that the mechanical stability of the highly porous supraparticles was suitable for practical applications. Highly porous unitary (ZnO, SiO_2), binary (TiO_2 – ZnO, TiO_2-Au, ZnO-Au), and ternary (TiO_2-ZnO-Au) supraparticles can be easily achieved by simply changing the composition of the inorganic phase (Fig. 5f-k). This confirms the possibility for integrating multiple functions into a single supraparticle for optimized applications.

The Péclet number (*Pe*) is a relevant parameter describing the evaporation process of a suspension. *Pe* evaluates the relative contributions of advection and diffusion to the motion of the colloidal particles. Droplet evaporation on a superhydrophobic surface is radially symmetric, and the driving force for internal particle motion is attributed to particle diffusion and advection caused by the shrinkage of the gas-liquid interface, which makes *Pe* applicable to this isotropic evaporation configuration. For evaporating spherical droplets, *Pe* is the ratio of the typical time t_d required for colloidal particles to diffuse through the initial droplet radius and characteristic evaporation time t_{ev}. t_d is related to the droplet size and diffusion coefficient (D_p) of colloidal particles, and can be expressed as

$$t_d = R_0^2/D_p \tag{20}$$

For a spherical particle with stick boundary conditions, D_p can be estimated using the Stokes-Einstein relation

$$D_p = k_B T/(6\pi\eta r) \tag{21}$$

where η and r represent the suspension viscosity and radius of the

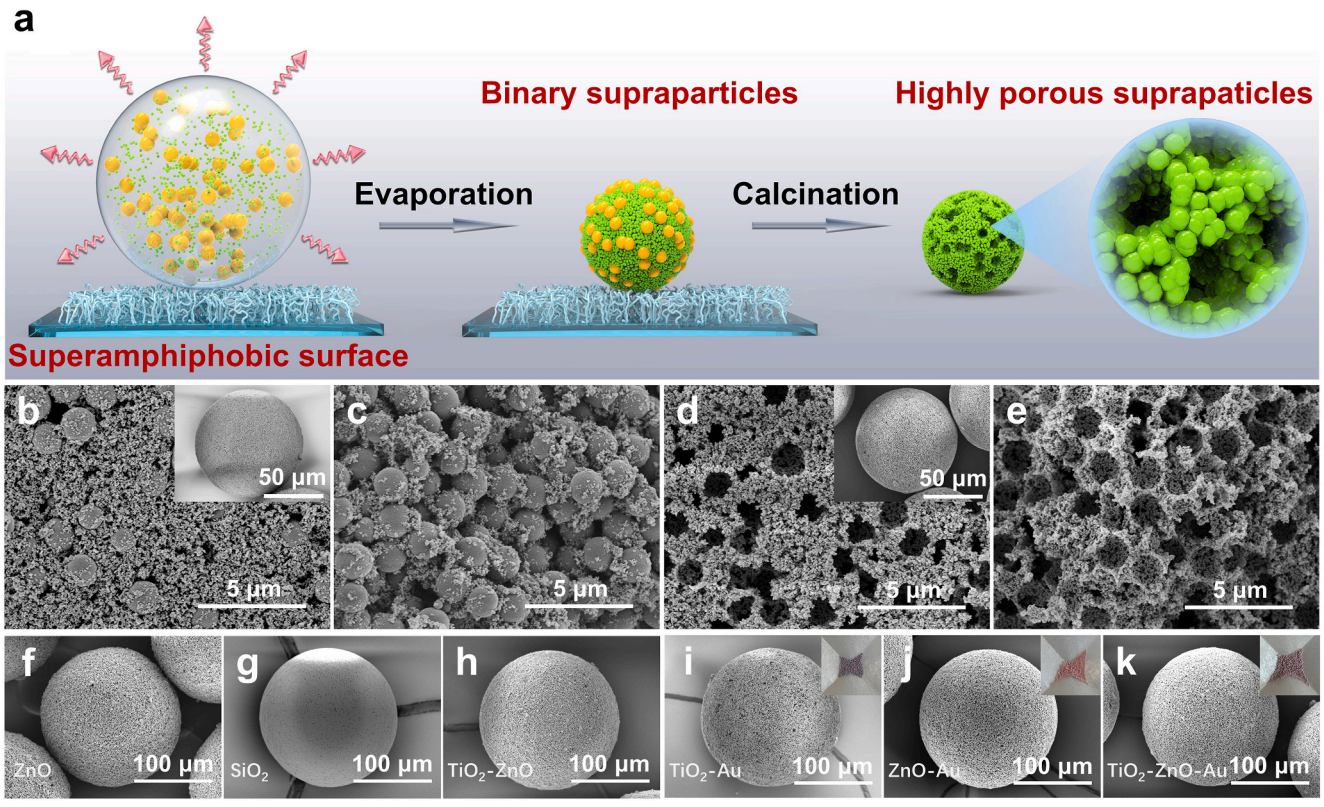

Fig. 5. Tuning the porosity of supraparticles. (a) Schematic of porous supraparticle formation mediated by droplet evaporation and post-calcination. (b-e) SEM images of the surface (b, d) and inner part (c, e) of binary TiO_2 – PS (b, c) and highly porous TiO_2 (d, e) supraparticles. Insets (b) and (d) show the whole binary and porous supraparticle, respectively. (f-k) SEM images of ZnO, SiO_2, TiO_2 – ZnO, TiO_2 – Au, ZnO – Au, and TiO_2 – ZnO – Au porous supraparticles. Insets are optical images of the hybrid supraparticles. Reproduced under terms of the CC-BY license [94]. Copyright 2019, The Authors, published by American Chemical Society.

colloidal particle, respectively. The suspension viscosity can be estimated in conjunction with the solvent viscosity η_S using the following formula [113].

$$\eta = \eta_S(1 + 2.5\phi + 5.913\phi^2) \tag{22}$$

The characteristic evaporation time is given by

$$t_{ev} = R_0/v_{ev} \tag{23}$$

where R_0 and v_{ev} represent the initial droplet radius and rate of gas-liquid interface shrinkage, respectively. Therefore, by combining Eq. (2), we find that the Péclet number of colloidal particles for evaporating spherical droplets, which is independent of the initial droplet radius, is given by

$$Pe = t_d/t_{ev} = \frac{1}{2}\left(\frac{3}{4\pi}\right)^{2/3}\frac{\Lambda}{D_p} \tag{24}$$

The *Pe* of colloidal particles for co-dispersed droplets of the same material is related to their particle diameter and evaporation rate. We observed the stratification behavior of particles in an isotropic evaporation configuration by evaporating co-dispersed droplets containing 338 nm and 1.43 μm PS colloidal particles (with volume fractions of 2.5 % and 5.5 %, respectively) on superamphiphobic surfaces at 23 °C with a relative humidity of 24 %, and we fabricated core-shell structured supraparticles (Fig. 6a) [79]. The small particles were enriched on the surface and assembled into a close-packed crystalline shell (~20 μm thick) with point and line defects, whereas large particles occupied the core (Fig. 6a). The shrinkage of the gas-liquid interface caused by droplet evaporation induces particle concentration gradients within the droplet, which result in a chemical potential gradient acting on the colloidal particles. Owing to the difference in *Pe* between the two types of particles, the gradient exerted a strong driving force on the large particles, pushing them away from the gas-liquid interface towards the center of the droplet. In contrast, small particles congregate on the surface during evaporation and assemble into crystalline shell structures (Fig. 6b). The theoretical simulation results are consistent with the experimental results (Fig. 6c), which demonstrate that the composition of the particles regulates the structure of the supraparticles.

Rastogi et al. constructed different supraparticles by adjusting the composition of primary particles in the evaporating droplets [28,92].

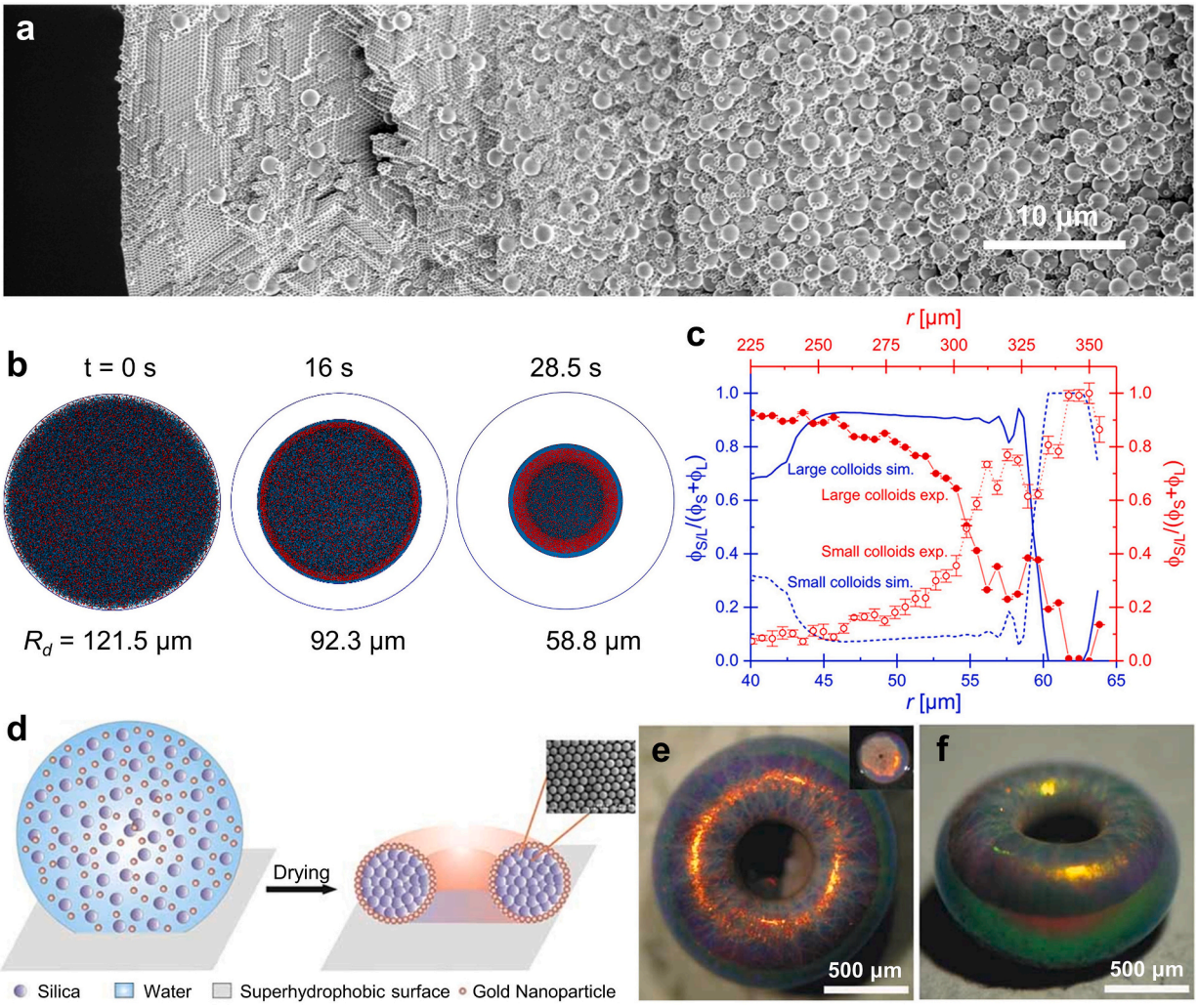

Fig. 6. Supraparticles are determined by components. (a) SEM image of a supraparticle formed from a bidisperse colloidal suspension during "fast" evaporation. (b) Simulation of a bidisperse colloidal suspension in a fast evaporation drop ($\Lambda = 1046$ μm^2/s) at various times. (c) Relative volume fractions of colloids after evaporation from simulations (blue) and experiments (red) for fast evaporation ($\Lambda = 1046 \pm 20$ μm^2/s). Reproduced under terms of the CC-BY license [79]. Copyright 2019, The Authors, published by American Chemical Society. (d) Schematic of supraparticle formation by evaporating a droplet containing suspension of silica and gold (Au) nanoparticles. (e) Top and angled view of "golden doughnut" supraparticles fabricated from a droplet containing 330 nm silica and 22 nm Au particles. Reproduced with permission [92]. Copyright 2010, Wiley-VCH. (For interpretation of the references to color in this figure legend, the reader is referred to the web version of this article.)

Doughnut-shaped supraparticles were obtained by evaporating co-dispersed droplets containing SiO_2 (330 nm) and Au (22 nm) nanoparticles on a superhydrophobic surface [92]. By controlling the volume ratio of the particles inside the droplets, the thickness and strength of the shell formed by particles aggregated at the gas-liquid interface during evaporation, thereby enabling the droplets to form a doughnut-shaped supraparticle by shape collapse at the late stages of evaporation. Particles of different sizes segregate, resulting in doughnut-shaped supraparticles with a core-shell structure. The relatively large SiO_2 nanoparticles occupy the inner core of the supraparticle, whereas the Au nanoparticles form the shell structure (Fig. 6d). As-prepared core-shell structured supraparticles exhibited color diffraction patterns of photonic crystals (Fig. 6e) under the synergistic effect of the hexagonal close-packed structure formed by the inner SiO_2 and the light-absorbing property of the Au nanoparticles in the shell. This provides a practical basis for constructing different core-shell/anisotropic structured supraparticles using a one-step drying process.

3.1.3. External magnetic field

The application of an external magnetic field is an effective way to regulate the structure of the supraparticles when magnetic particles are present in the evaporation system. When magnetic particles are introduced as additive components, the applied external magnetic field can induce the directional migration of magnetic particles within the droplets, which leads to multiphasic supraparticles. Rastogi et al. evaporated bidisperse colloidal droplets composed of colloidal PS particles and magnetic (Fe55/Ni45) nanoparticles on a superhydrophobic surface using an external magnetic field to construct heterogeneous supraparticles with a discrete distribution of magnetic particles. The effects of the magnitude and distribution of the external magnetic field on the assembly of magnetic particles were verified through theoretical simulations [92]. As shown in Fig. 7a, placing a single magnet above an evaporating droplet can aggregate the magnetic particles in the upper part of the supraparticle to form a Janus structure. Through the anisotropic magnetic response of the Janus structure, the external magnetic field can further drive the motion of the supraparticles and assemble them into a hexagonal close-packed array, which can then be used as a remotely manipulated drug delivery system for precise targeting. Further control of the magnetic field by adjusting magnets around the droplets can affect the number of magnetic patches formed in the supraparticles (Fig. 7b,c). These bi-patch and tri-patch supraparticles provide a novel tool for efficient mixing in microchannels. In addition, it serves as an ideal model for an in-depth investigation of the patchy anisotropic supraparticles.

In addition to constructing heterogeneous supraparticles, droplets containing magnetic particles under an external magnetic field can exhibit properties similar to those of magnetic fluids and form different morphologies [95]. Hu et al. successfully prepared a series of supraparticles with anisotropic shapes, including cone, barrel, and double-tower-like structures, by evaporating the dispersion droplets of superparamagnetic Fe_3O_4 nanoparticles under an external magnetic field (Fig. 7d) [32]. The droplets exhibited isotropic evaporation in a magnetic field of 16 kA/m at an early stage. As the water evaporated, the concentration of the internal particles increased. Eventually, anisotropic supraparticles formed under the combined effects of droplet confinement and the driving force of the external magnetic field. Fig. 7e shows the transition of the supraparticle morphology as the particle concentration changes from 1 to 30 wt% under a magnetic field of 16 kA/m. When the concentration $\leq$ 6 wt%, supraparticles form cone-like structures with different sizes and aspect ratios. When the concentration $\geq$ 12 wt%, barrel-like supraparticles with hollow interiors and top-to-bottom continuity are formed because of the combined effect of buckling and dewetting (Fig. 7e). The magnetic field strength had a significant effect on the morphology of the supraparticles. When the magnetic field strength increases to 160 kA/m, cone-like supraparticles can still form even when the particle concentration $\leq$ 12 wt%. However, droplets with concentrations $\geq$21 wt% split at the top and form two cones as evaporation proceeds, ultimately forming two-tower-like supraparticles (Fig. 7f). The angle of the double-tower structure depends mainly on the orientation of the applied external magnetic field. This method allows for the facile synthesis of supraparticles with specific structures and magnetic responsive properties.

3.1.4. Other conditions

In addition to the aforementioned factors, the morphology and structure of supraparticles are also affected by other conditions [96–102]. Zhou et al. realized supraparticles with different morphologies by modulating the dynamic behavior of the three-phase contact

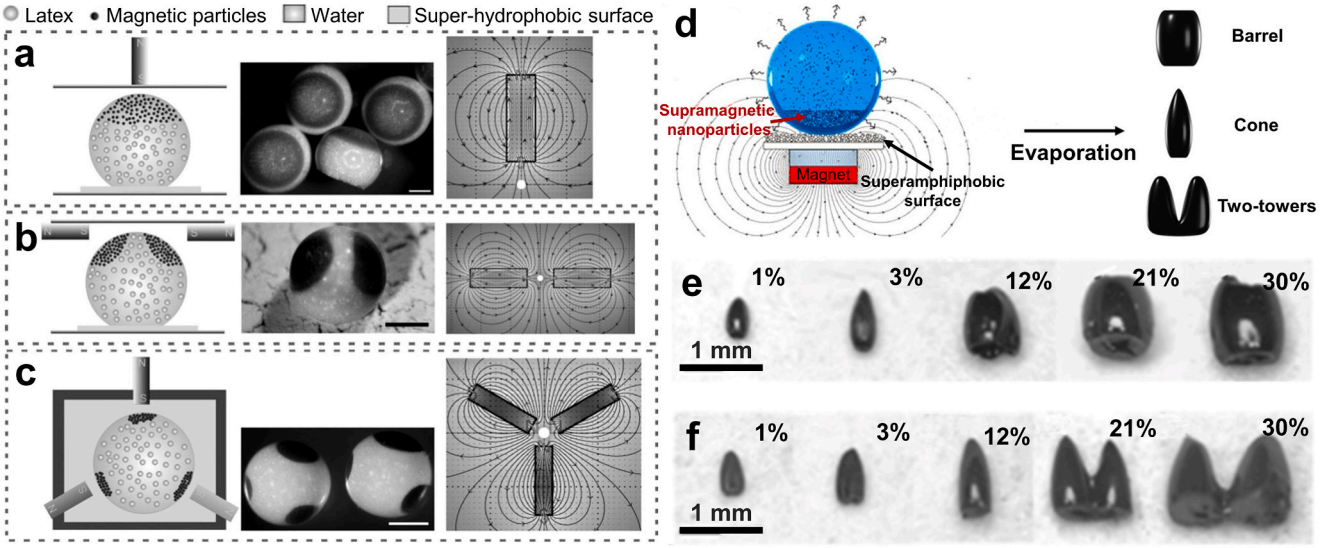

Fig. 7. External field-assisted supraparticle fabrication. (a-c) Schematics of the assembly configuration, optical micrographs, and simulation patterns of applied external magnetic fields for (a) single patch, (b) bi-patch, and (c) tri-patch magnetic supraparticles. The scale bars are 500 μm. Reproduced with permission [92]. Copyright 2010, Wiley-VCH. (d) Schematic of shaping the assembly of superparamagnetic nanoparticles with a magnetic field. (e, f) Optical photos of supraparticles prepared with different nanoparticle concentrations under magnetic field of 16 (e) and 160 kA/m (f), respectively. Reproduced under terms of the CC-BY license [32]. Copyright 2019, The Authors, published by American Chemical Society.

line [101]. As shown in Fig. 8a, the concentration of colloidal particles in the droplets containing poly(styrene-methyl methacrylate-acrylic acid) colloidal particles on a superhydrophobic surface increased linearly with evaporation when the initial particle concentration reached a relatively high level of 40 wt%. The particles agglomerate and form a thick shell to maintain the evaporation rate, which results in the continuous shrinkage of the three-phase contact line and formation of spherical supraparticles. The internal particle concentration no longer increased linearly when the initial particle concentration was reduced to 10 wt%, formed a shell structure. Further evaporation caused the shell to collapse, pinning the three-phase contact line and anisotropic evaporation rates, which drive the particle assembly to form buckled structures. Introducing ethanol into a droplet at a concentration of 40 wt% reduced the surface tension, causing partial contact line pinning on the surface, which led to asymmetric shrinkage. Contact-line pinning occurred in one direction, whereas uniform shrinkage occurred in the perpendicular direction. The asymmetric shrinkage behavior became more pronounced with increasing ethanol content, driving the assembly of particles to form anisotropic ellipsoid-like structures. Modifying the three-phase line shrinkage behavior enhances the diversity of supraparticle morphologies, which helps expand its applicability in nonbleaching pigments and full-color display pixels.

Harraq et al. investigated the effect of the aspect ratio of particles within a droplet at a low concentration (0.01 volume fraction) during assembly [98]. The supraparticle structure changed from buckled to spherical when the ratio of the rod-shaped to spherical particles was adjusted. When the concentration of particles inside the droplet was low, the particles aggregated at the gas-liquid interface under the dual action

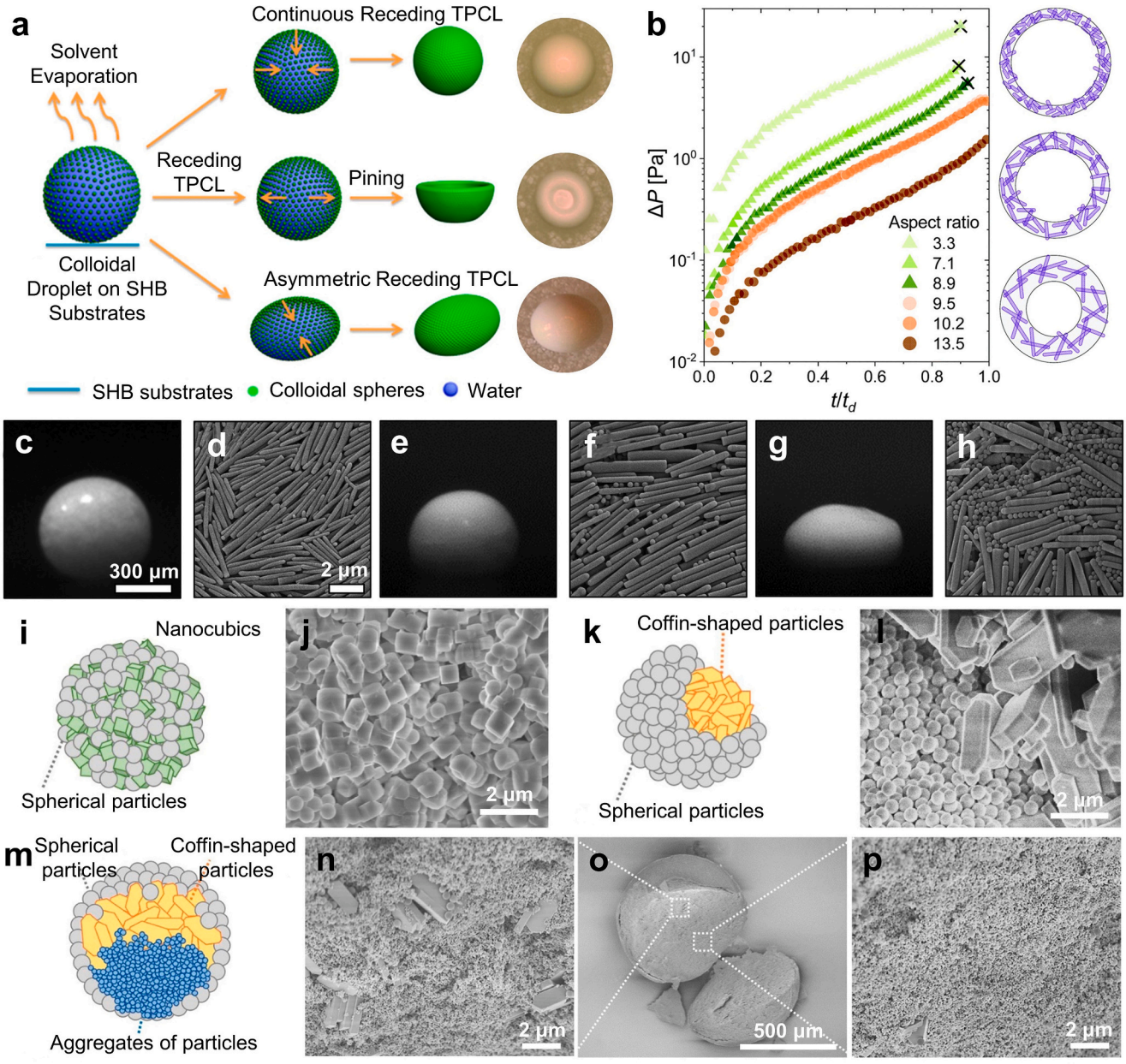

Fig. 8. (a) Controllable fabrication of supraparticles by dynamic three-phase contact line behaviors, including continuous receding, receding and then pinning, and asymmetric receding of the TPCL. Reproduced with permission [101]. Copyright 2015, American Chemical Society. (b) Change in the pressure drop across the shell, calculated throughout drying for droplets containing different aspect ratio rods. (c-h) Optical and SEM images of dried shells containing (c, d) 0, (e, f) 0.5, and (g, h) 5 sphere-to-rod number ratios, respectively. Reproduced with permission [98]. Copyright 2020, Royal Society of Chemistry. (i-p) Schematics and SEM images of well-mixed assembly of supraparticle (i, j), core/shell supraparticle by size effect (*k*,*l*), Janus core/shell structured supraparticle (m-p). Reproduced under terms of the CC-BY license [100]. Copyright 2021, The Authors, published by MDPI.

of advection and diffusion, thereby increasing the pressure drop inside and outside the shell. The shell deforms and generates non-spherical supraparticles when the mechanical strength of the shell is insufficient to counteract the pressure drop. This deformation phenomenon is pronounced when monodisperse spherical particle dispersion droplets were used because such particles are more accessible to form close-packed ordered structures, which significantly reduces the permeability of the shell and generates a more significant pressure drop. Introducing building blocks with a large aspect ratio, such as rod-shaped structures, can help maintain this buckling behavior. As shown in Fig. 8b, pressure drops after the formation of the assembled shell decrease with the increasing aspect ratio of the building blocks because the smaller the aspect ratio, the closer is the stacking behavior of the rod structure to that of spherical particle, and the tighter is the formed shell. In contrast, building blocks with large aspect ratios are unlikely to achieve orientation consistency, which results in a jamming structure formed by rod-shaped structures. This jamming structure had a higher permeability than spherical particles with a small aspect ratio, which significantly reduces the pressure drop and helps avoid the formation of non-spherical supraparticles. Therefore, the permeability of the assembled shell structure and the supraparticle morphology can be controlled by mixing high-aspect-ratio silica nanorods with spherical silica nanoparticles and controlling the ratio in the dispersion. As shown in Fig. 8c-h, the obtained supraparticles transformed from spherical to buckled non-spherical structures by increasing the amount of introduced spherical particles while maintaining a constant concentration of rod-shaped particle, and the degree of buckling showed a positive correlation with the number of spherical particles. Thus, adjusting the aspect ratio of the primary particles provides a feasible strategy for constructing supraparticles with controllable morphology at low concentrations.

In addition to the aspect ratio, Shim et al. achieved controlled fabrication of heterogeneous supraparticles with well-mixed core-shell and Janus core-shell structures by manipulating the shape, size, and dispersity of the building blocks [100]. Unlike the size of the building blocks and dispersity of particles in the droplets, merely changing the shape of the building blocks (with smaller aspect ratios) did not significant affect the morphology or structure of the supraparticles. The evaporation process did not produce any concentration differences when well-dispersed, and similarly-sized particles were used as building blocks, allowing for the formation of supraparticles with uniformly distributed primary particles. As shown in Fig. 8i, j, mixing silica nanoparticles (D = 533 ± 10 nm) and zeolites nanocubes (D = 670 ± 140 nm) with the same volume concentration resulted in supraparticles with a uniform distribution of both particles. Core-shell supraparticles formed based on the differential effects of evaporation on particles when there was a significant difference in size between the primary particles, i.e., silica nanoparticles (D = 533 ± 10 nm) and coffin-shaped zeolite NPs (long axis: 3.8 ± 2.2 μm, short axis: 1.3 ± 0.8 μm, and thickness: 380 ± 220 nm) (Fig. 8k). The small silica nanoparticles are enriched at the surface, forming a dense shell, whereas the large zeolite particles are distributed inside the supraparticles, creating a distinct boundary between them (Fig. 8l). Further, particle dispersity showed the same effect. Mixing well-dispersed silica nanoparticles with poorly dispersed TiO_2 nanoparticles (20–30 nm) at the same concentration resulted in the aggregation of TiO_2 particles to form a core structure, while silica remained in a dispersed state near the gas-liquid interface and created a shell structure, thereby yielding core-shell supraparticles. This provides a new strategy to construct composite supraparticles with small particles as the core and large particles as the shell. Furthermore, introducing poorly dispersed particles into a well-dispersed binary dispersion enabled the synthesis of a ternary core-shell supraparticle with a Janus core under the synergistic effect of size and dispersity (Fig. 8m). Fig. 8n-p show the supraparticle structure obtained by mixing TiO_2 with a dispersion of silica and coffin-shaped zeolites. Silica nanoparticles formed a shell, with the inner core comprising zeolites and TiO_2, thereby creating a Janus structure. These results further elucidate the role of building blocks in the assembled supraparticles and offer a practical basis for constructing various supraparticles with different shapes and functions by selecting appropriate building blocks.

As a platform for droplet evaporation, superhydrophobic substrates can impose confinement effects on droplets, controlling the morphology of the supraparticles. Sperling et al. realized the controllable preparation of patchy anisometric and ellipsoidal silica supraparticles on a V-shaped superhydrophobic surface by precisely controlling the shape and spatial orientation of the supraparticles [96]. Compared with flat superhydrophobic surfaces, V-shaped superhydrophobic surfaces provide specific confinement conditions to regulate the evaporation process, enhancing the uniformity of the prepared supraparticles and effectively controlling the direction of their extension. As shown in Fig. 9a, the colloidal silica droplet automatically positioned itself at the center of the V-shaped opening structure on the V-shaped superhydrophobic surface, showing two contact points between the droplet and the substrate (i). Owing to the restriction of vapor diffusion by the substrate, the evaporation rate perpendicular to the substrate was lower than that of the free part of the droplet that was not in contact with the substrate (ii). Therefore, on the free side of the droplet, the droplet shrinks rapidly because of evaporation. The aggregation behavior of the internal particles at the interface was more significant than that of the droplet in contact with the substrate, which resulted in a change in the droplet symmetry and stretching along the direction perpendicular to the curved channel (iii). This anisotropic stretching continued until the droplets were completely dry, forming anisotropic ellipsoidal silica supraparticles. This achieves the directional deformation of the apparent morphology of supraparticles based on superhydrophobic substrates (iv). In this process, the degree of curvature of the substrate determines the anisotropy of the evaporation rate during droplet evaporation. Further, the opening angle of the V-shaped surface directly affects the deformability during droplet evaporation. In addition, changing the ionic strength in the colloidal droplet to control the interaction between the colloidal particles can further adjust the aggregation behavior of the particles during evaporation. Combined with the confinement effect of the V-shaped surface, this method provides an opportunity to design and construct supraparticle materials with specific anisotropy.

Oguztürk et al. combined a magnetic field with a curved superhydrophobic surface to construct reinforced anisometric patchy supraparticles with self-propelling properties [97]. Colloidal droplets containing silica and Fe_3O_4@Pt particles were evaporated onto a V-shaped superhydrophobic surface (Fig. 9b) to obtain self-propelling supraparticles with stable mechanical properties. The curved substrate drives the assembly of the primary particles to form an anisometric structure with silica constituting the main body of the supraparticles, whereas the magnetic Fe_3O_4@Pt particles aggregate towards the magnetic field side, forming heterogeneous supraparticles with magnetic and catalytic properties at one end. The Fe_3O_4@Pt particles comprising the magnetic ends of the supraparticles can catalyze the decomposition of hydrogen peroxide (H_2O_2) to produce oxygen, which enables the self-propelled motion of the supraparticle in a hydrogen peroxide solution. Furthermore, the addition of sodium silicate (Fig. 9c,d) and microfibrillated cellulose (MFC) (Fig. 9e,f) to the system enhanced the interaction between the building blocks, effectively preventing the destruction of the supraparticle caused by the generation of oxygen from the catalytic reaction. Thus, the structural stability and lifespan of the self-propelled supraparticles are guaranteed, providing a basis for the fabrication of structurally stable self-propelling materials.

3.2. Supraparticle preparation mediated by evaporation on lubricant surface

The evaporation on lubricant surfaces is a practical approach for preparing supraparticles. Lubricant surfaces demonstrate very low contact angle hysteresis for incompatible liquids, because of their micro/nanostructures are filled with low-surface-energy lubricants. The

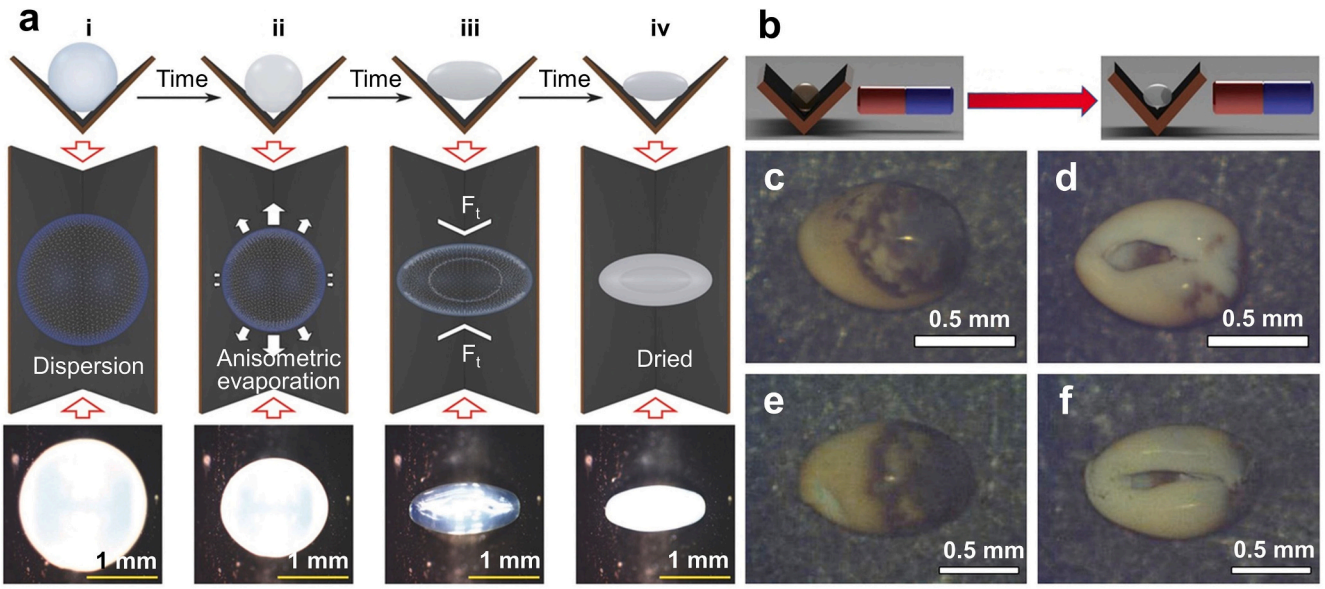

Fig. 9. Curved superhydrophobic surface mediated fabrication of anisometric supraparticles. (a) Mechanism and optical images of anisotropic evaporation on bent superhydrophobic surface. (i) Homogeneously distributed dispersion droplet sitting within the cleft of the bending. (ii) Anisotropic evaporation attributed to blocking the droplet sides. (iii) Stronger FS particle collection on the droplet open sides promotes droplet elongation. (iv) Shape retention during further shrinking to final dried FS supraparticle. Reproduced with permission [96]. Copyright 2017, Wiley-VCH. (b) Scheme for preparing patchy supraparticles in the presence of magnets. (c-f) Microscopy images of the front (c, e) and back (d, f) side of Na_2SiO_3 associated FS-based (c, d) and MFC & Na_2SiO_3-associated FS-based (e, f) supraparticles. Reproduced with permission [97]. Copyright 2021, Wiley-VCH.

lubricant prevents the liquid from infiltrating the substrate while forming a wetting ridge at the periphery of the droplet. The pinning of the droplet edges on the substrate was effectively suppressed during evaporation, driving the assembly of internal building blocks to form supraparticles using the droplet as a template. Gao et al. prepared a lubricant surface by coating a hydrophobic substrate with silicone oil and explored the particle assembly process to achieve controllable fabrication of asymmetric supraparticles [38]. The silicone oil ascended along the droplet when the colloidal particle dispersion droplets were deposited on the lubricant surface. Two contact lines were formed: liquid-liquid-air (LLA) and liquid-liquid-solid (Fig. 10a). The bottom edge of the droplet was surrounded by an oil ridge that inhibited evaporation at the bottom edge. Water evaporates only from the uncovered top of the droplet, resulting in anisotropic evaporation. For a 0.05 μL colloidal droplet of PS (2.5 μm in diameter) with a volume concentration of 0.015 %, the bottom edge of the droplet continuously retracts during the initial stage of evaporation (< 280 s). Anisotropic evaporation drives an upward liquid flow inside the droplet, disturbing the dispersion of primary particles and driving the aggregation of particles at the water-air and water-oil interfaces rather than deposition. As evaporation proceeded, an increasing number of particles aggregated at the water-oil interface and temporarily settled into the LLA. Some particles may escape and move downward along the water-oil interface. When these particles reached the bottom edge of the droplet, they move inward with droplet edge retraction. In the final evaporation stage (280–390 s), most colloidal particles at the interface are extruded into a viscous colloidal shell, and the droplet edge begins to pin onto the substrate. With continuous water loss, the fully stacked shell gradually sinks until it is deposited on the substrate. Finally, anisotropic supraparticles are formed on the surface (Fig. 10b) because of the lubricant interlayer between the liquid and substrate. Solid particles are prevented from being anchored to the substrate, making supraparticle collection easier by solvent rinsing. Using this method, the controlled construction of anisotropic TiO_2, ZnO, SiO_2, carbon diamond, and other supraparticles can be achieved easily (Fig. 10c-g).

Kim et al. introduced a surfactant (cetyltrimethylammonium bromide, CTAB) into TiO_2 dispersion droplets to alter the apparent morphology of anisotropic supraparticles [5]. CTAB reduced the surface tension of the dispersion droplets and increased friction at the contact line. Before reaching the critical micelle concentration (CMC), the apparent contact angle of the droplet decreased gradually with increasing surfactant concentration. The increase in the initial contact diameter and contact line friction of the droplet made it difficult for the contact line to shrink during evaporation. The apparent anisotropic characteristics of droplet evaporation increased, realizing control of the anisotropic supraparticle morphology (Fig. 10h). With an increase in the surfactant concentration, the evident receding contact angle of the droplet decreased from 105° (without CTAB) to 75° (2 mM CTAB), and the contact diameter increased from 1305 to 1840 μm. The ratio of the contact line moving distance to the initial contact diameter decreased gradually from 0.6 to 0.35 when preparing supraparticles with (Fig. 10i-l) mushroom-shaped, hemispherical, convex lens-shaped, and disc-shaped morphologies.

Recently, Jiao et al. applied lubricant surfaces for the high-throughput fabrication of supraparticles by mediating the evaporation of colloidal dispersion droplets using lubricant dot arrays prepared on superamphiphobic surfaces [114]. First, a superamphiphobic surface (WCA = 155°) was prepared by spraying TiO_2 with a fluorocarbon surfactant mixture. A hydrophobic pattern was obtained by treating the surface with UV light (WCA = 143°). Subsequently, the patterned surface was impregnated with a lubricant to obtain a lubricated dot array with a superamphiphobic background (water sliding angle (WSA) = 20°). After deposition on the surface, the droplets were bound to the lubricated dot array for evaporation because of the difference in surface wettability between the patterned area and the background. Except for cases in which the droplet size was too large, or the lubricant dot was too small, the lubricant formed an oil ridge in the droplet periphery and underwent the same evaporation process as that of conventional lubricant substrates, thus obtaining anisotropic supraparticles. The morphology of the supraparticles can be modulated by synergistically controlling the diameter of the lubricant dots and droplet volume. Benefiting from the spatial confinement effect of the lubricant surfaces, this strategy achieved a high-throughput preparation of supraparticles, with 42 supraparticles on a single surface (76.2 mm × 25.4 mm) and a

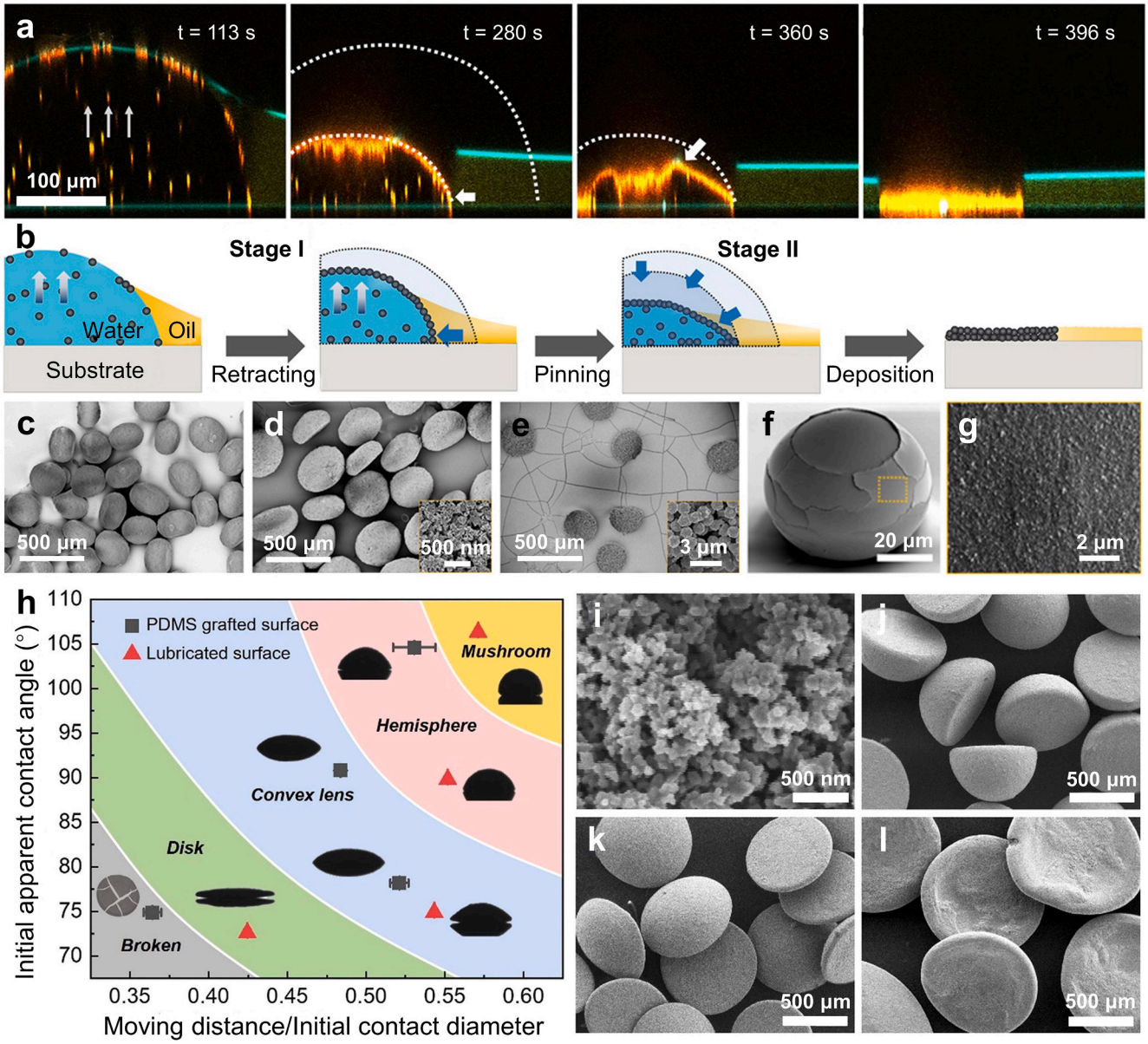

Fig. 10. Evaporation on the lubricant surface mediated supraparticle fabrication. (a) Snapshots of colloidal droplets evaporating on oil-coated hydrophobic. (b) Schematic of the droplet evaporation on the oil-coated surface. (c-e) Oblate supraparticles obtained by (c) TiO_2, (d) ZnO, and (e) SiO_2, respectively. Insets in (d, e) show the porous structures. (f-g) Morphology (f) and surface structure (g) of carbon diamond supraparticles with a nearly spherical shape. Reproduced under terms of the CC-BY license [38]. Copyright 2019, The Authors, published by American Chemical Society. (h) Shape diagram for supraparticles synthesized by different apparent contact angles, ratios of moving distances, and initial contact diameters of dispersion droplets. (i) Magnified SEM image of TiO_2 supraparticle of (j). (j-l) SEM images of synthesized supraparticles of (j) mushroom shape, (k) convex lens shape, and (l) disk shape. Reproduced with permission [5]. Copyright 2021, Elsevier.

total mass of 147 mg. Heterogeneous supraparticles with magnetic and catalytic properties were achieved by evaporating binary droplets containing Fe_3O_4 and TiO_2 nanoparticles, and the methylene blue degradation efficiency under UV irradiation reached 98.2 %. The catalysts can be rapidly recycled with the help of a magnetic field, which is a reliable strategy for the high-throughput preparation of supraparticles.

Ouzo is a Greek anise-flavored aperitif composed of water, ethanol, and anise oil. Ethanol evaporates preferentially during the evaporation of Ouzo droplets, resulting in a decrease in oil solubility (Ouzo effect). Therefore, phase separation occurs at the contact line where the oil droplets were initially formed. Researchers developed a novel self-lubricating evaporation method to construct supraparticles. Tan et al. dispersed colloidal particles into ternary droplets composed of water (39.75 vol%), ethanol (59.00 vol%), and anise oil (1.20 vol%), and performed droplet evaporation on a hydrophobic surface to construct anisotropic porous TiO_2 supraparticles [31]. As shown in Fig. 11a, Ouzo droplets containing colloidal particles formed a spherical cap structure on the surface. As the evaporation proceeded, ethanol evaporated faster than water, leading to the precipitation of anise oil in the droplet. An oil ring formed beneath the droplet, constituting a self-lubricating substrate (Fig. 11b, c). When the as evaporation was complete, solid supraparticles were obtained (Fig. 11d, e). Laser scanning confocal microscopy further clarified the self-lubricating processes of droplet evaporation and nanoparticle self-assembly. Different phases were distinguished by adding xylene (for the oil phase) and rhodamine 6G (for the water phase) to the initial droplets, and a series of horizontal scans were performed at about 10 μm above the substrate to track the formation of the oil ring. Fig. 11a-e illustrates the dynamic evaporation

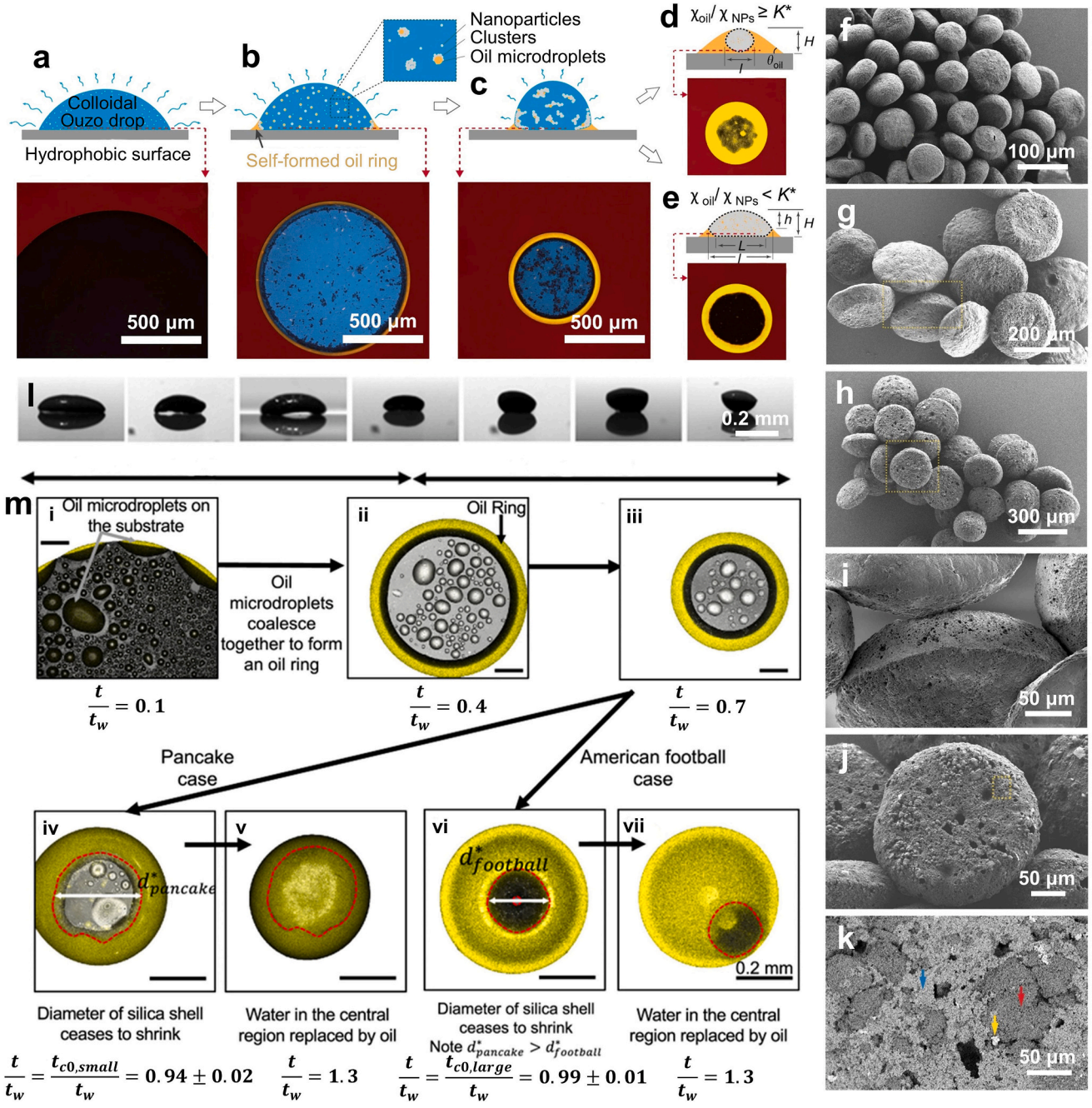

Fig. 11. Supraparticle assembly through self-lubricating evaporating colloidal ouzo drops. (a-e) Illustrations of "self-lubrication" and corresponding confocal photographs. Color indications under a confocal microscope: yellow, oil; blue, water/ethanol; black, clusters of nanoparticles; red, substrate. (a) The initial state of ouzo droplet with well-dispersed nanoparticles. (b) Oil ring formation mediated prevention of nanoparticle deposition at the contact line. (c) Shrinkage of the oil ring sweeps nanoparticles/clusters from the substrate, and the generated supraparticles either float on the residual oil (d) or sit on the substrate (e). (f–k) SEM images of the generated porous TiO_2 supraparticles (f), TiO_2-SiO_2 binary supraparticles (g, i), and TiO_2-SiO_2-Fe_3O_4 ternary supraparticles (h, j, k). Reproduced under terms of the CC-BY license [31]. Copyright 2019, The Authors, published by Springer Nature. (l) Submillimeter-sized supraparticles were obtained after the evaporation of colloidal droplets. The shape changes from pancake-like (leftmost) to American football-like (rightmost) with an increasing size of particles. (m) Supraparticle formation visualized by confocal microscopy, (i) Initially, the oil microdroplets are formed on the substrate due to the phase separation of oil. (ii) Oil microdroplets coalescence, forming the oil ring. (iii) The oil ring contracts in diameter as the liquids evaporate. (iv − vii) At $t = t_{c0}$, the shell stops contracting. However, $t_{c0,small} < t_{c0,large}$, and consequently, the final diameters of the shell are different for the two cases: $d^*_{pancake}$ (iv and v) is larger than $d^*_{football}$ (vi and vii). Reproduced under terms of the CC-BY license [25]. Copyright 2021, The Authors, published by American Chemical Society. (For interpretation of the references to color in this figure legend, the reader is referred to the web version of this article.)

process, where blue, yellow, black, and red represent the aqueous solution, phase-separated oil, nanoparticles (clusters), and hydrophobic substrate, respectively. At the onset of evaporation, there was no significant phase separation in the droplet, and the nanoparticles were highly dispersed (Fig. 11a). As evaporation proceeded, the nanoparticles aggregated through mutual interactions. The nucleated oil microdroplets were attached to the nanoparticles (clusters) owing to the preference for heterogeneous nucleation on the surface over homogeneous nucleation in the liquid phase. After the nucleation of the microdroplets, more nanoparticles attached to the oil-water interface.

Meanwhile, the nucleated oil microdroplets coalesced to form an oil ring at the edge of the droplet, preventing the aggregation of nanoparticles (clusters) at the air-oil-substrate contact line (Fig. 11b). As the droplet shrank, the oil ring was forced to slide inward, driving the assembly of the internal particles to form three-dimensional supraparticles (Fig. 11c). The oil ring gradually shrunk until the droplet was suspended on the surface and the final morphology of the supraparticles was formed. The ridges of the oil ring wrapped around the edge of the colloidal droplet, with its inner ridge forming the lower half of the dynamic template for nanoparticle self-assembly. The liquid-air interface constitutes the upper half, where supraparticles are formed, driven by oil-wetted ridges. Thus, different evaporation configurations can be obtained by adjusting the oil concentration in the mixture (resulting in oil-wetted ridges of various sizes), which generates supraparticles with distinct morphologies, as shown in Fig. 11d, e. Additionally, by controlling the type of nanoparticles, monocomponent (TiO_2, Fig. 11f), binary (TiO_2-SiO_2, Fig. 11g,i), and ternary (TiO_2-SiO_2-Fe_3O_4, Fig. 11h,j,k) supraparticles could be easily prepared. During evaporation, some oil droplets remained within the droplets and assembled into particles. After the supraparticles were formed, the oil slowly escaped from the supraparticles, forming pore structures with a porosity exceeding 90 % (Fig. 11i-k). Thus, this supraparticle construction strategy is effective for constructing porous catalytic materials.

Raju et al. investigated the effect of the colloidal particle size on the morphology of supraparticles based on a self-lubricating droplet evaporation strategy [25]. As shown in Fig. 11l, seven spherical silica colloidal particles with sizes ranging from 20 nm to 1 μm were integrated into Ouzo droplets for supraparticle fabrication. With the variation in colloidal particle size, the size of the supraparticles in the horizontal direction decreased with an increase in the number of building blocks and exhibited various shapes. When the diameter of the colloidal particles was less than 100 nm, the supraparticles exhibited a "pancake" shape; conversely, colloidal particles with diameters larger than 100 nm formed an "American football" shape. In situ monitoring of the evaporation of the Ouzo droplet indicated that the supraparticle assembly depended on the creation of a flexible colloidal particle shell at a fast-moving interface. As shown in Fig. 11m, as evaporation proceeded, silica nanoparticles assembled at the oil-water interface to form a flexible shell with a lateral width, which continuously decreased and adjusted its shape according to the shape of the oil-water interface. After a certain period, the shell transitioned from flexible to rigid and ceased shrinking (Fig. 11m,iv&vi). The size of the building blocks determines the duration of the transitions. When the size of building blocks is large, the shell deformation stopped at the ceasing time ($t_{c0,large}$), where $t_{c0,large}/t_w = 0.99 \pm 0.01$, close to the time of evaporation of all water (Fig. 11m,vi); on the other hand, for small-sized colloidal particles, the shell stops deforming at an early ceasing time, $t_{c0,small}$, where $t_{c0,small}/t_w = 0.94 \pm 0.02$. Simultneously, water remained in the central region of the droplet (Fig. 11m,iv). After the shell composed of small building blocks stops shrinking ($t_{c0,small} = 0.94t_w$), it can no longer conform to the oil-water interface. Therefore, with further water evaporation, most silica particles accumulated at the air-water interface, eventually forming pancake-shaped supraparticles ($t = t_w$). However, for larger building blocks with $t_{c0,large} = 0.99t_w$, the shell remained consistent with the oil-water interface until the end (t_w), resulting in a considerable number of particles at both the air-water and oil-water interfaces, which led to the formation of football-shaped supraparticles. Furthermore, the bottom diameters of the pancake-shaped supraparticles were larger than those of the football-shaped supraparticles ($d^*_{pancake} > d^*_{football}$, Fig. 11m, iv&vi). The evaporation of self-lubricating droplets provides a basis for constructing supraparticles of various shapes and sizes.

Recently, Heo et al. established a large-scale supraparticle fabrication strategy with the simultaneous regulation of the supraparticle size by confining Ouzo droplets using hydrophilic patterns of different sizes constructed on a hydrophobic surface [115]. PDMS brushes were grafted onto a common substrate to obtain a hydrophobic surface owing to their excellent liquid repellency and low contact angle hysteresis. Then, the hydrophobic layer was treated with oxygen plasma under masking to decompose the exposed PDMS into circular hydrophilic micropatterns of different sizes (50, 100, 300, and 500 μm). Finally, the Ouzo droplets containing the colloidal silica particles evaporated on the surface. The hydrophilic patterns confined the Ouzo droplets to specific regions, enhancing the fabrication throughput, while their sizes could be adjusted by contact line shrinkage driven by the Ouzo droplet oil ring, regulating the final size of the supraparticles. This approach enabled rapid and large-scale fabrication of supraparticles with diameters of 21 $\pm$ 3, 141 $\pm$ 1, 79 $\pm$ 4, and 99 $\pm$ 3 μm, respectively, providing a simple and high-throughput droplet evaporation-mediated supraparticle construction model for practical applications [115].

4. Applications of supraparticles fabricated by droplet evaporation

Supraparticles allow the assembly of nanoparticles into larger solid structures, enabling easier material handling and recovery while reducing the hazards associated with the high mobility of nanoparticles [116]. As an agglomerate, a supraparticle combines the basic functionalities of nanoparticles, such as a high specific surface area, intrinsic material properties, and catalytic activity, and enhances functionality through synergism, coupling, and co-localization, surpassing the simple functional sum of the primary structural units. Therefore, supraparticles demonstrate potential applications in catalysis [94,117], sensing [118–120], efficient delivery [116,121], optical applications [65,122,123], carbon dioxide capture [124].

4.1. Catalytic applications

The large porosity and specific surface area of supraparticles can provide more reaction sites and enhance material transfer efficiency. Meanwhile, supraparticles can effectively protect functional materials from damage by the external environment, endowing them with good prospects in catalysis.

Enzymes can efficiently catalyze many biological reactions in living organisms and artificial reaction systems. Enzyme-catalyzed cascade reactions reduce the activation energy of reactions and avoid side reactions caused by the cooperation of multiple enzymes and their high specificity, thereby improving the chemical reaction rate while ensuring high catalytic efficiency and throughput. Compared to the dispersed systems, using supraparticles as enzyme/enzyme carriers shorten the substance transfer distance between the enzymes and carriers. They possess large specific surface areas, accelerate substance transfer, and significantly improve the efficiency of cascade reactions. Jo et al. constructed multimodal enzyme-carrying supraparticles for rapid and visual glucose detection by evaporating silica nanoparticle dispersion droplets carrying glucose oxidase (GOx) and horseradish peroxidase (HRP) on a lubricant surface [117]. GOx catalyzes the oxidation of glucose to gluconic acid generating H_2O_2. HRP oxidizes potassium iodide (KI) to produce iodine by consuming H_2O_2, which resulted in solution coloration and the formation of a glucose sensor (Fig. 12a). The efficiency of cascade reactions catalyzed by enzyme-carrying supraparticles is 2.9 times higher than that of enzyme-carrying nanoparticle dispersion systems (2.7×10^{-4} mM/s) because of the confinement effect of the supraparticle on the enzyme-carrying particles and the enhanced accessibility of reactants to enzymes attributed to the porous structure. The prepared enzyme-carrying supraparticles could be used for glucose diagnosis based on enzyme-cascade reactions. As shown in Fig. 12b, a mixture of urine from diabetic patients and a KI solution was dropped onto enzyme-carrying supraparticles for glucose detection, and the glucose content of different samples was determined using a commercial glucometer. After 20 min, the urine samples from patients with diabetes turned brownish-yellow, corresponding to glucose levels of #1: 484 mg/

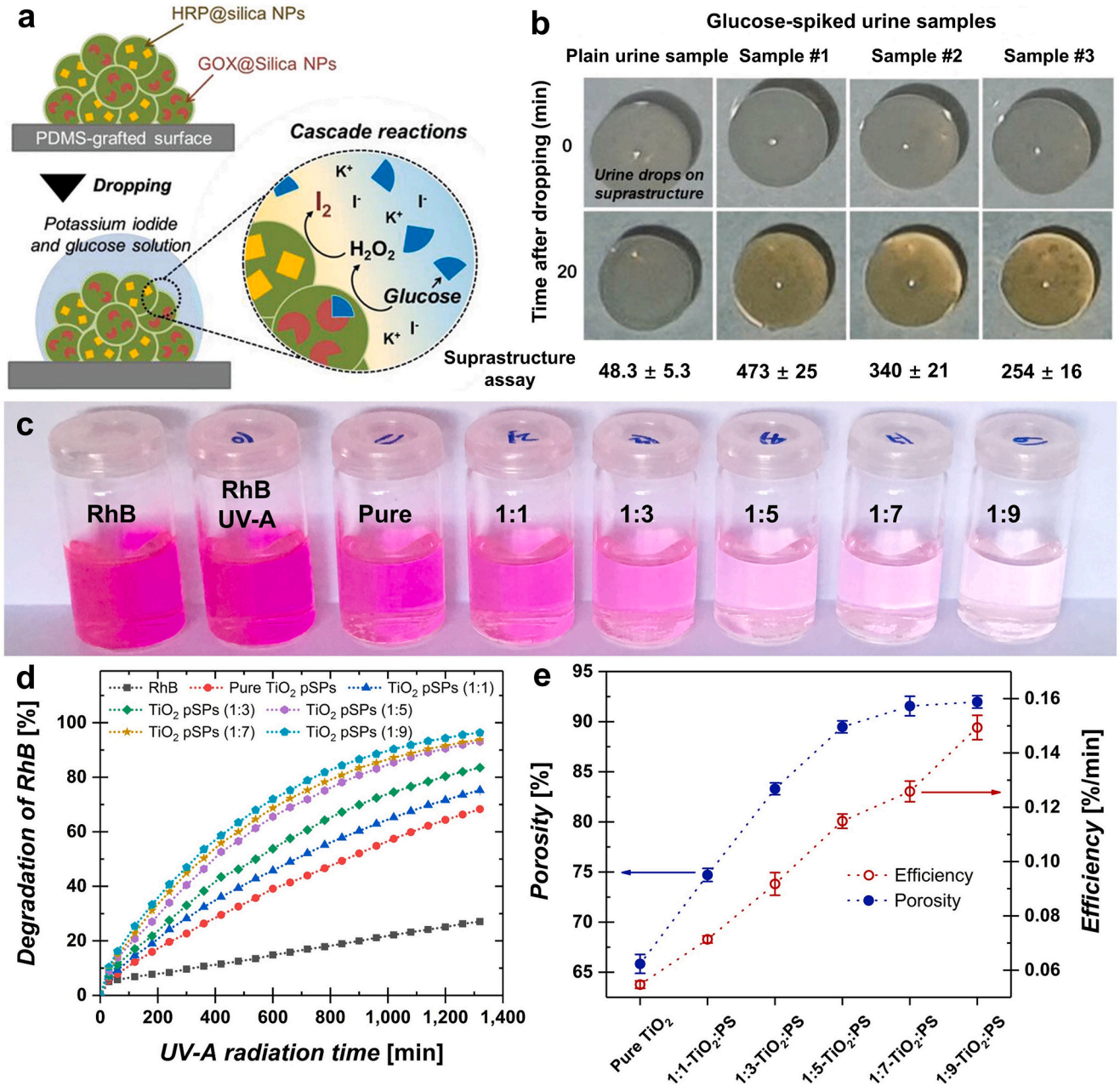

Fig. 12. Catalytic applications of supraparticles. (a) Schematics for the supraparticle-based glucose assay. (b) Glucose assay for human urine samples. The generation of a yellow-brown color after 20 min indicates the progression of reactions. Reproduced with permission [117]. Copyright 2022, Wiley-VCH. (c) Optical image of rhodamine B (RhB)/supraparticle solutions after exposure to UV-A for 22 h. (d) Relationship between the degradation of RhB and irridation time for supraparticles with different porosities. (e) Relationship between photocatalytic efficiency and porosity. Reproduced under terms of the CC-BY license [94]. Copyright 2019, The Authors, published by American Chemical Society. (For interpretation of the references to color in this figure legend, the reader is referred to the web version of this article.)

dL, #2: 343 mg/dL, #3: 268 mg/dL (Fig. 12b). In contrast, the normal urine samples showed almost no color change within 20 min, falling within the range of normal glucose levels (37.3 mg/dL). Thus, visual glucose diagnosis based on enzyme-carrying supraparticles was achieved. Further integration with Nanodrop spectroscopy to measure the absorbance of enzyme-carrying supraparticles reacting with different concentrations of glucose and KI solutions at 250–450 nm yielded a standard curve for glucose determination. Compared to measurements obtained using a commercial glucometer, the glucose content error was only ±5 %, which enabled the accurate quantitative analysis of glucose content in urine samples at the diagnostic level, making the enzyme-carrying supraparticles a promising biosensor.

In addition to enzyme catalysis, the porous structure of supraparticles can effectively enhance the diffusion of reactants or products, improving their performance in practical applications, such as heterogeneous catalysis. In a previous study, we constructed TiO_2 supraparticles with a high porosity and used them for the photocatalytic degradation of Rhodamine B [94]. First, TiO_2-PS binary supraparticles were obtained by evaporating droplets of organic-inorganic binary (PS-TiO_2) colloidal dispersions on a superhydrophobic surface. Subsequently, the PS phase was removed by calcination, resulting in TiO_2 supraparticles with hierarchical porous structures. The porosity of TiO_2 supraparticles was controlled by adjusting the volume ratio of TiO_2 to PS in the evaporating droplets, and a maximum porosity of 92.1 % was

achieved. The combination of macropores derived from the PS templates and mesoporous structures formed by the self-assembly of TiO_2 nanoparticles effectively enhanced the mass transfer efficiency inside and outside the supraparticles, resulting in an increase in the photocatalytic degradation efficiency of Rhodamine B with an increasing porosity of equal mass TiO_2 supraparticles (Fig. 12c, d). The photocatalytic activity of the supraparticles with maximum porosity was approximately 2.7 times higher than that of the supraparticles without macropore structures (Fig. 12e). This study provides a new strategy for preparing highly porous materials and high-performance catalysts, further expanding the applications of supraparticles in catalysis.

4.2. Sensitive SERS detection

Surface-enhanced Raman spectroscopy (SERS) substrates are another important application of supraparticles in the development of rapid and highly sensitive detection techniques for ultra-low analyte concentrations [125–127]. Compared to a traditional flat substrate, Zhizhchenko et al. proved that a structured substrate could significantly enhance the sensitivity of SERS analysis [128]. They fabricated a central superhydrophilic trap structure encircled by periodically aligned superhydrophobic columns on the surface of a bulk polytetrafluoroethylene substrate, employing a rapid and straightforward direct femtosecond pulsed filament-assisted ablation technique. The considerable lateral size of the center trap prevented the transition of the deposited droplets to the Wenzel state, preventing the fixation of the three-phase contact line until the droplet has completely evaporated, thereby achieving the smallest contact area diameter in the Cassie-Baxter state and allowing the analyte molecules to be concentrated and deposited in the designated area. The structure enables the efficient deposition of rhodamine dye dissolved in 10^{-10} M in 5 μL water droplets onto a 90 × 90 μm^2 target. The proposed texture provided a concentration factor of 10^3 mm, which is one order of magnitude higher than that of the previously reported surface textures. Furthermore, the surface can serve as a multifunctional biosensing platform that can detect the fingerprints of deposited analyte molecules through SERS enhancement, with an estimated detection threshold surpassing 10^{-15} mol·L^{-1}. Compared to typical one-dimensional and two-dimensional nanostructures, employing three-dimensional assembled supraparticle as SERS substrates offers great advantages such as a larger hotspot volume, higher surface area, and higher hotspot density, which present broad prospects in fields such as food safety, environmental protection, and bioanalysis [129–131]. Cao et al. achieved three-dimensional Au@Ag supraparticles by evaporating core-shell Au@Ag nanoparticle dispersion droplets and utilizing them as SERS substrates to detect thriams and antibiotics [119]. The evaporation of droplets drives the

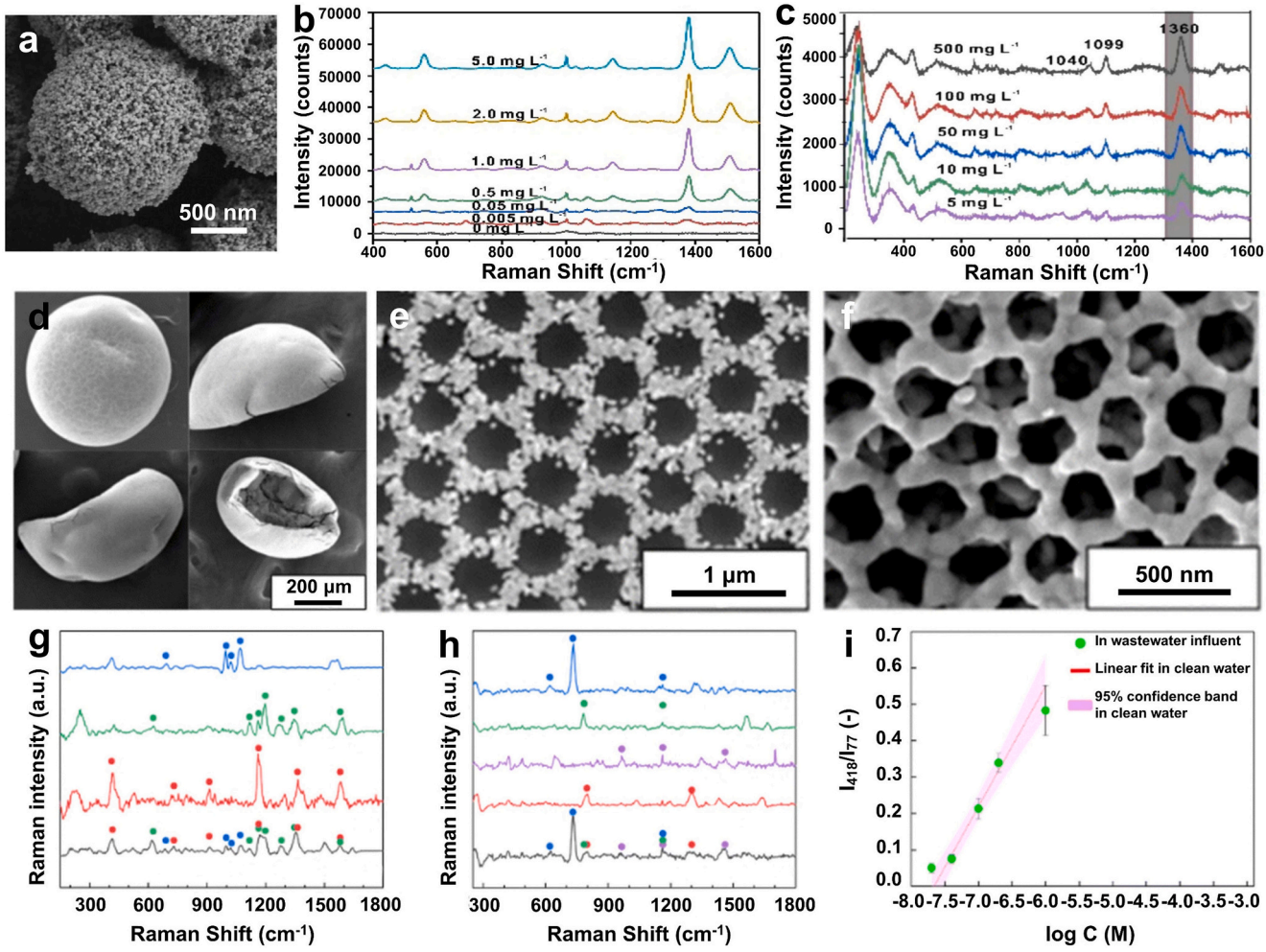

Fig. 13. Sensing applications by employing supraparticles as SERS substrates. (a) SEM images of 3D Au@Ag supraparticles. (b, c) SERS spectra of thiram (b) and CTR (c) on 3D supraparticle-based substrates after incubation with solutions of different concentrations. Reproduced with permission [119]. Copyright 2023, Elsevier. (d-f) SEM images of four-side views (top, left, bottom, right, clockwise) of binary PS-Au supraparticles (d), binary supraparticle surface (e), and porous Au supraparticle surface after calcination (f). (g, h) Multiplex SERS detection of environmental contaminants and SERS detection in an environmental matrix of a mixture solution containing MGITC, RhB, BZT, and a mixture solution containing adenine, thymine, guanine, and cytosine. (i) Sensitivity test for MGITC detection in wastewater influent with different concentrations. Reproduced with permission [118]. Copyright 2022, Royal Society of Chemistry.

internal particle assembly to form millimeter-sized supraparticles (Fig. 13a), with each supraparticle containing over 10^4 Au@Ag nanoparticles forming numerous three-dimensional hotspots. Moreover, the non-close-packed assembly structure facilitated the diffusion of more target molecules towards the hotspots, enhancing the interaction and providing higher sensitivity.

The 3D supraparticle SERS substrate exhibited excellent SERS sensitivity when detecting thiram in the 0.005–5.0 mg/L range. As shown in Fig. 13b, even at the limit of detection (LOD) of thiram (0.005 mg/L, 20 nM), the characteristic Raman peak of the target molecule (1380 cm^{-1}) could still be observed. The three-dimensional porous structure endowed the supraparticle-derived SERS substrate with higher sensitivity than those of the conventional three-dimensional multilayer stacking structures, whose sensitivity increased by approximately 8-fold. Moreover, the non-close-packed assembly structure ensured the uniformity of the hotspots on the surface of the supraparticles. The relative standard deviation (RSD) between different sampling points of the same supraparticle was 13.7 %, and the RSD between different supraparticles was only 9.3 %, which confirms the reliability of using supraparticles as SERS substrates for detection. In addition to thiram, the prepared supraparticles exhibited excellent antibiotic detection performance. Fig. 13c shows the SERS spectra at different concentrations of ceftriaxone sodium (CTR). Significant characteristic Raman peaks of CTR (1360 cm^{-1}) could still be obtained at low concentrations. Calculating the CTR adsorption curve revealed that the LOD for CTR could reach 1.0 mg/L, further demonstrating the enhanced detection sensitivity.

Kang et al. obtained porous Au supraparticles as SERS substrates for environmental pollutant detection [118]. First, binary hollow dome-shaped supraparticles were fabricated by liquid droplet evaporation on a superhydrophobic surface using Au nanoparticles (diameter of approximately 43 nm) and PS particles (diameter of roughly 600 nm) as building blocks (Fig. 13d). In the binary supraparticles, the PS particles were assembled into a hexagonal close-packed structure, whereas the Au nanoparticles filled the gaps between the PS particles, forming an ordered patterned structure on the surface of the supraparticles (Fig. 13e). After calcining at 500 °C, the organic phase was removed, leaving porous supraparticles composed entirely of Au nanoparticles (Fig. 13f). The resulting shell-like structure of the supraparticles effectively shortened the diffusion distance, enabling the target molecules to adsorb rapidly onto the gold surface and improve the response speed. Combined with the large pore structure and high porosity generated under the inorganic to organic phases ratio of 1:9, the supraparticles exhibited excellent SERS performance, with the LOD for Malachite green isothiocyanate (MGITC), RhB, benzenethiol (BZT), atrazine (ATZ), adenine, and an oligonucleotide gene segment were 41.0 nM, 98.4 nM, 1.8 μM, 37.7 μM, 1.7 μM, and 1.0 μM, respectively, indicating their broad applicability for pollutant detection. The prepared supraparticles enabled multiplex SERS detection because of the differences in the characteristic Raman peaks of different pollutants. As shown in Fig. 13g, h, using gold supraparticles as SERS substrates helped realize the detection of mixtures of MGITC, RhB, BZT, and four nucleotides (adenine (A), thymine (T), guanine (G), and cytosine (C)). Characteristic peaks of each component in both mixtures were observed in the SERS spectra. They can be used to quantitatively detect components, demonstrating the performance of porous gold supraparticle multiplex SERS substrates for environmental pollutants. Furthermore, SERS detection of MGITC in pure water and wastewater using porous gold supraparticles showed a positive linear correlation between the characteristic intensity at 418 cm^{-1}. Each data point of the logarithm of the concentration in wastewater fell within the 95 % confidence interval of the calibration curve of MGITC in pure water (Fig. 13i). These results indicate that wastewater had limited interference on the SERS performance of the porous supraparticles, proving the utility of the prepared supraparticles as SERS substrates for environmental analysis.

4.3. Drug delivery

The properties of supraparticles, such as large pore volumes and surface areas, render them ideal delivery vehicles. The large size of the assembled structures effectively reduces the hazards associated with nanomaterials because of their high mobility and non-specific surface activity while retaining the properties of the building blocks [132].

Mattos et al. used biogenic silica ($BSiO_2$) as building blocks and cellulose nanofibers (CNFs) as binders to construct stable supraparticles by evaporating binary colloidal droplets on a superhydrophobic surface, which were then used for the efficient delivery of green biomolecules (thymol) to the soil [116]. As a simple and green construction strategy, droplet evaporation allows the rapid (approximately 10 min) formation of spherical supraparticles at 60 °C. The main structure of the supraparticles was constructed using $BSiO_2$ particles with a high specific surface area (~350 m^2/g), whereas CNFs with unique properties such as biodegradability, high aspect ratio, strength, and stiffness formed a three-dimensional network structure interspersed between the $BSiO_2$ particles and interacted with the particles through hydrogen bonding, endowing the supraparticles with high porosity and strength. Uniaxial compression tests showed that the fracture force of supraparticles prepared with 5 wt% CNFs reached 1.25 N, indicating ideal mechanical strength and effectively addressing the toxicological and environmental issues arising from structural damage in the carrier systems. As a carrier system, the drug molecule thymol can be loaded into the supraparticle structure through various methods such as pre-loading, in situ loading, and post-loading without significantly affecting the mechanical performance (Fig. 14a). Different loading methods also affect loading efficiency. As shown in Fig. 14b, in situ loading resulted in a low loading capacity of ~12 mg/g due to the volatility of the biomolecules during liquid droplet evaporation. Pre-loading was limited by the encapsulation efficiency of $BSiO_2$, which achieved a loading capacity of 40 mg/g. However, post-loading resulted in a larger loading capacity of 80 mg/g because of the aggregation of molecules in the interstices of the supraparticles. Therefore, different loading methods can be selected based on the requirements of the carrier systems, and the operational flexibility provides a broader range of applications. In addition to the loading capacity, the release of carrier systems determines their application performance. As shown in Fig. 14c, the delivery systems constructed using different loading strategies exhibited similar release curves, with the total amount of thymol released into water proportional to the initial payload. The release of thymol underwent two distinct stages: rapid release within the first 12 h, followed by slow release from 12 to 170 h (Fig. 14c). After 170 h, none of the delivery systems reached equilibrium, indicating that the use of supraparticle structures for delivery could achieve long-term, sustained release of payloads. In addition, as a carrier of the assembly structure, the supraparticle can protect the internal payloads and reduce photo-degradation caused by light exposure. After 24 h of visible light irradiation, thymol retention in the supraparticle delivery system, nanoparticle carrier system, and thymol solution was 100 %, 60 %, and 15 %, respectively. After 72 h of irradiation, thymol retention in the supraparticle system was 65 %, which was more than twice that of the nanoparticle carrier system, further confirming that supraparticle delivery systems can effectively enhance the long-term biological activity or bioavailability of specific payloads.

Wang et al. prepared mesoporous silica supraparticles using droplet evaporation and loaded them with the therapeutic protein, brain-derived neurotrophic factor (BDNF) for sustained inner-ear drug delivery [121]. As illustrated in Fig. 14d,e, mesoporous silica with a diameter of 400 nm was used as the building block, and silica supraparticles were prepared via controlled evaporation by dispersing droplets on a paraffin film surface. Then, annealing was carried out at 650 °C to enhance the mechanical stability of the supraparticles. Subsequently, BDNF was loaded onto the supraparticles to create a therapeutic protein delivery system. The assembled spherical supraparticles inherited the bimodal pore structure of mesoporous silica with sizes of 2–3 and 15–30

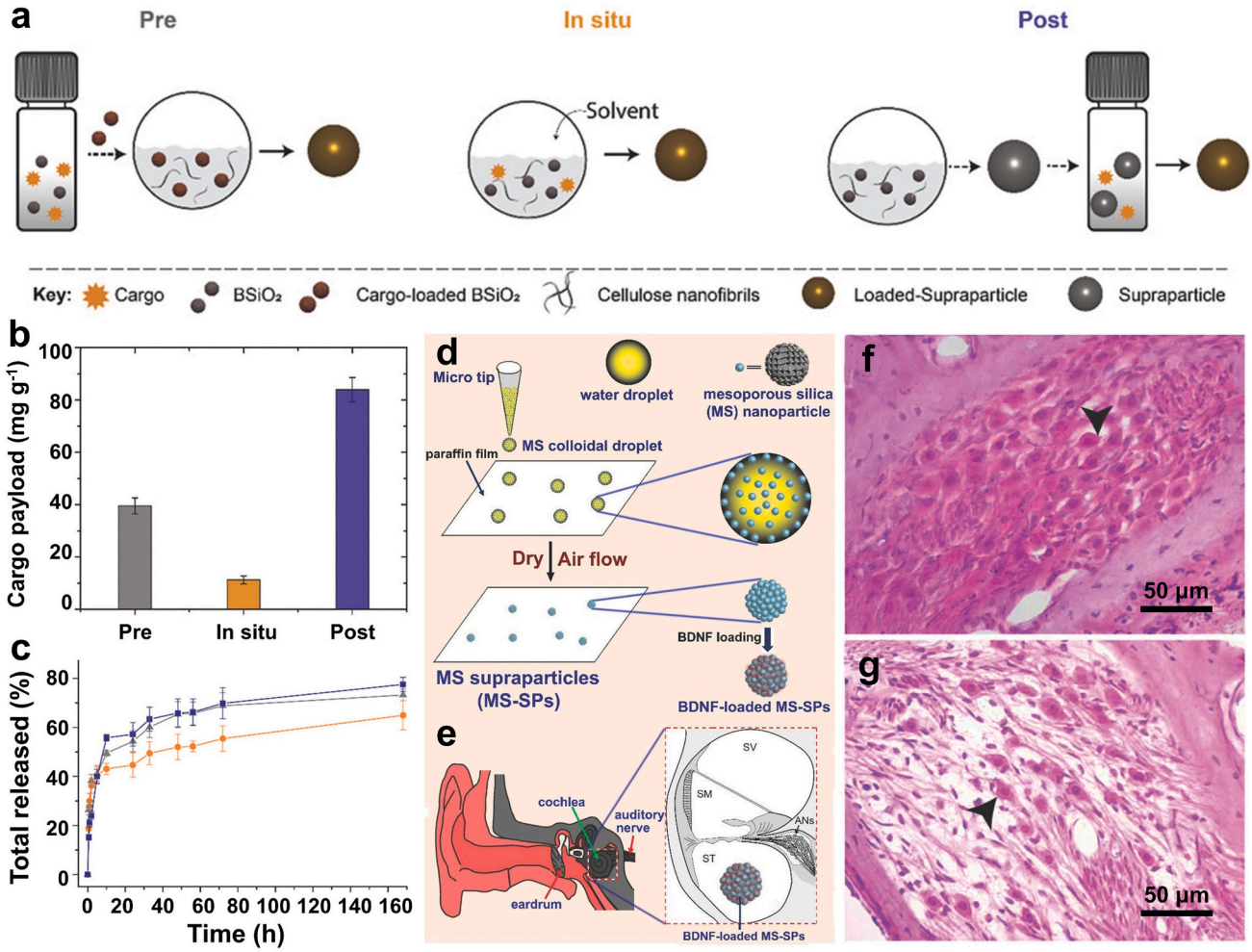

Fig. 14. Drug delivery mediated by supraparticles. (a) Schematic of the loading methodologies employed to form the bio-based biocidal superstructures. Three distinct cargo loading strategies were demonstrated. (b) Thymol payload in the superstructured biocides as a function of methods for loading. (c) Biocide release profiles normalized to the mass of thymol. Reproduced with permission [116]. Copyright 2018, Wiley-VCH. Schematic of (d) the preparation of mesoporous supraparticles and (e) surgical implanting of supraparticles in the inner ear. (f, g) Histological images of a cochlea from a profoundly deafened guinea pig treated with (f) BDNF-loaded and (g) unloaded supraparticles. The arrowheads indicate surviving ANs (primary auditory neurons). Reproduced with permission [121]. Copyright 2014, Wiley-VCH.

nm, whereas the stacking of particles formed large pores and channel structures of 100–200 nm. The presence of this hierarchical pore structure endowed the supraparticles with a surface area of 888 m^2/g and a pore volume of 2.0 cm^3/g, facilitating the transport of bio-macromolecules throughout the supraparticles and providing a high surface area for loading various sizes of drugs, such as small molecules, proteins, and nucleic acids. Post-loading of BDNF showed that the drug loading capacity of individual supraparticles with a size of 580 μm reached 1.33 μg. The delivery system achieved long-term sustained release through interactions between the supraparticles and BDNF. In a release test that lasted 70 days, BDNF exhibited rapid release in the first month, followed by a gradual decrease until completion. Histological images of the guinea pig cochlear treated with BDNF-loaded and unloaded supraparticles for 28 days in a cochlear perforation model are shown in Fig. 14f, g. The survival rate of primary auditory neurons (ANs) in the cochlea treated with BDNF-loaded supraparticles was higher, with a density of 1302 AN/mm^2 (Fig. 14f), which was 2.7 times higher than that of the control group (484 AN/mm^2, Fig. 14g). This implies that the supraparticle delivery system is suitable for implantation into the injured cochlea, and that the amount of BDNF released reaches the therapeutic level required for neuronal survival. Moreover, long-term sustained release ensures continuous drug delivery to injured tissues, guaranteeing the time required to repair the injured neurons. Therefore, it can alleviate the effects of surgical trauma and preserve the residual hearing and primary auditory neuron populations during cochlear implantation.

4.4. Optical applications

Supraparticles, as assemblies of building blocks, can self-assemble monodisperse colloidal particles into crystal arrays, thereby providing an effective tool for manufacturing advanced functional materials. The periodicity of the building blocks in supraparticles at the micro- and sub-micronscales endows these artificial structures with light-manipulation capabilities similar to those of natural opals (three-dimensional photonic crystals). Controlling characteristics such as long-range ordering, maximum packing density, well-defined pore size, and high surface-to-volume ratio of the particles enables the use of these supraparticles in photonics, light scattering, anti-reflection, and other optical fields [133–136].

Rastogi et al. mixed monodisperse colloidal PS particles of different sizes with Au nanoparticles with a diameter of 22 nm and obtained PS-Au opal supraparticles [29]. As illustrated in Fig. 15a, the small Au nanoparticles filled the gaps between the PS microspheres during droplet evaporation, which increased the effective refractive index between the microspheres and enhanced light reflection while reducing

back-scattering, thus producing high-contrast structural colors. As the diameter of the PS microspheres increased from 420 to 1000 nm, the size of the colored rings on the supraparticle surface decreased, whereas the number of rings increased with the PS diameter. Supraparticles assembled from 320 nm PS colloidal microspheres displayed only a blue ring. In contrast, supraparticles with larger diameter building blocks produced blue, green, yellow, and red rings, thereby realizing the regulation of supraparticle reflection bands in a controllable manner.

Lim et al. prepared buckled photonic microgranules using silica and carbon black nanoparticles as building blocks and Leidenfrost droplets as rapidly shrinking template [123]. As shown in Fig. 15b, an ethanol suspension containing SiO_2 and carbon black nanoparticles formed Leidenfrost drops on the surface at temperatures far above the boiling point of ethanol. Ethanol evaporated immediately from the bottom of the droplet, creating a vapor film between the droplet and surface. The vapor film no longer supported the remaining droplet, and the residual ethanol rapidly evaporated from the top surface of the droplet. Asymmetric evaporation caused the top surface of the droplet to buckle and form buckled supraparticles. Owing to the rapid evaporation in this method, SiO_2 particles do not have enough time to create an ordered assembled structure; instead, they accumulate into an amorphous structure, which exhibits strong incoherent multiple scattering and appears white. Therefore, carbon black nanoparticles were introduced to suppress whitening and enhance the color contrast. The photonic supraparticles prepared from Leidenfrost droplets were composed of a glassy packing of SiO_2 particles, and their structural color was angle-independent, allowing for the preparation of photonic supraparticles covering the entire visible range by simply varying the size of the SiO_2 particles. As shown in Fig. 15c-e, red, green, and blue photonic supraparticles were obtained using SiO_2 particles with diameters of 295, 256, and 190 nm, respectively. This angle-independent photonic supraparticle preparation process is rapid, with a stable optical color dependent on the supraparticle size. They are suitable alternatives to chemical or toxic dye materials for many practical coloration applications.

Bigdeli et al. constructed photonic crystal supraparticles with a spherical upper top and a cavity structure at the bottom by controlling the colloid droplet concentration and particle size (Fig. 15f-h) [65]. With the assembly of SiO_2 nanoparticles, the solid-liquid interface undergoes light scattering, and the wavelength of the reflected light increases with an increase in the assembled structure, causing a gradual color change of the interface from white to red, orange, yellow, and finally green. Therefore, the fabrication of anisotropic photonic supraparticles with different reflected light colors can be realized by adjusting the size of the building blocks (Fig. 15i), which promotes the development of various sensors based on spectral changes.

5. Conclusion and perspectives

The last decade has witness significant developments in supraparticle assembly mediated by droplet evaporation on

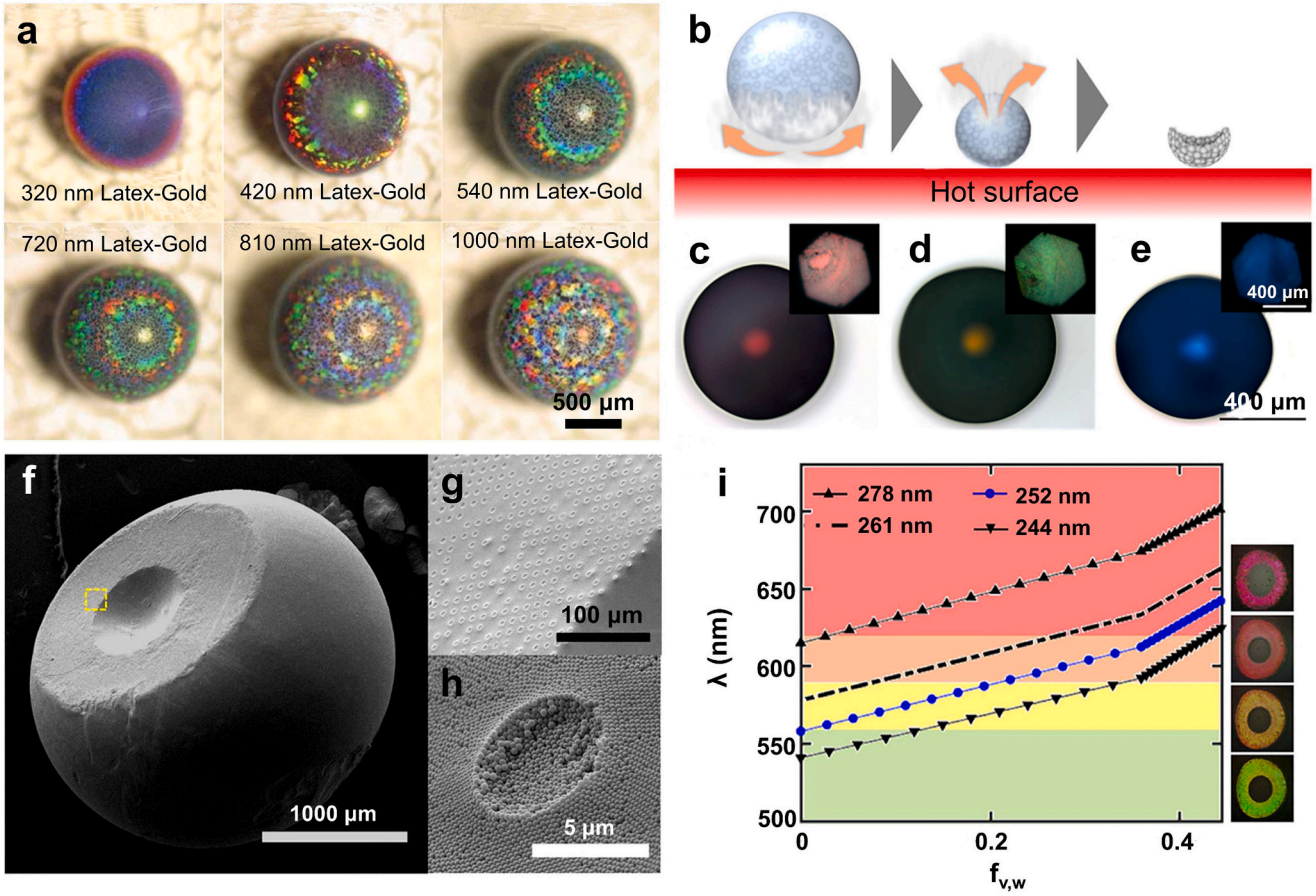

Fig. 15. Optical applications of supraparticles achieved by droplet evaporation. (a) Optical microscopy images of PS and Au nanoparticle opal supraparticles containing microspheres of varying sizes. Reproduced with permission [29]. Copyright 2008, Wiley-VCH. (b) Schematic illustration showing the formation of supraparticles confined by a Leidenfrost drop. (c-e) Optical microscopy images of photonic microgranules composed of three different diameters of silica particles: (c) 295 nm, (d) 256 nm, and (e) 190 nm. The inset image shows the top surface of each photonic microgranule. Reproduced with permission [123]. Copyright 2014, American Chemical Society. SEM images of the bottom of a dried NP-laden drop: (f) entire deposit, (g) footprints of micro-pillars in the flat region shown in (f), and (h) footprint of a single pillar. (i) Analysis of the reflected colors from the bottom view of an evaporating droplet. Reproduced with permission [65]. Copyright 2020, American Chemical Society.

superhydrophobic surfaces. Compared to traditional solvent-based methods used for constructing supraparticles, the droplet evaporation strategy effectively reduces the use of organic solvents, surfactants, template agents, and etc. The resulting supraparticles do not require complex postprocessing, including separation, treatment, purification, and so on, effectively avoiding damage to the primary particles caused by toxic reagents and processing, which helps reduce environmental pollution and energy consumption. Meanwhile, the boundary conditions of the assembly process can be controlled. Supraparticles with different structures and functions can be controlled with high repeatability by adjusting evaporation conditions such as temperature, humidity, particle concentration, composition, volume, and external field. Further, almost all building blocks are converted into products, dramatically enhancing the utilization of raw materials. These advantages of the droplet-evaporation-mediated supraparticle fabrication strategy significantly promote the application of supraparticles in various fields, such as catalysis, drug delivery, and optics. This has led to new research directions for constructing novel supraparticles, such as multi-component catalytic supraparticles, carbon-based supraparticles, and biological assemblies, further promoting the development of supraparticles in fundamental research and practical applications. However, the following limitations need to be addressed before applying supraparticles in practical scenarios.

I. The yield of supraparticles is a critical factor for practical application. The assembly of supraparticles is completed when individual droplets evaporate on superhydrophobic surfaces, and therefore, the yield of these supraparticles depends dramatically on the size of the superhydrophobic substrate and the rate at which uniform droplets are generated. Currently, the preparation of supraparticles using this method is limited to small quantities at the laboratory-scale, with a maximum of hundreds of supraparticles in a single run, which is insufficient for practical applications. Therefore, developing a prototype "supraparticle factory" is essential for continuously and efficiently producing uniform droplets in large quantities.
II. The size of supraparticles prepared by droplet evaporation is another limiting factor, particularly those prepared via droplet evaporation on superhydrophobic surfaces. Constructing spherical supraparticles on superhydrophobic surfaces requires the droplets to remain in the Cassie state during the evaporation process, requiring the droplets to maintain a spherical shape on the surface even when they are nearly completely dry. Currently, superhydrophobic surfaces rely on a combination of surface roughness and low surface energy materials, which result in relatively large protrusions and voids on the surface, limiting the miniaturization of the supraparticle size. Although researchers have developed candle-soot templates and nanofilament-based superhydrophobic surfaces that significantly reduce surface roughness, micrometer-scale pores are still required for maintaining superhydrophobicity. This makes supraparticles constructed on such surfaces with a minimum size of 10–50 μm, considerably larger than those built in the solution-phase. Therefore, developing superhydrophobic materials with microstructures or even bulk-phase materials it is of great significance, obtaining supraparticle materials with sizes comparable to those obtained by solution-phase methods and expanding the scope of the applications of supraparticles.
III. The assembly of supraparticles mediated by droplet evaporation relies on the capillary force generated by liquid evaporation to aggregate the building block particles, hydrogen bonds, and electrostatic interactions between the particles, without forming stable chemical bonds. Therefore, the mechanical stability of the prepared supraparticles is insufficient. Although some inorganic supraparticles, such as TiO_2, SiO_2, ZnO, and Au can be calcined to enhance stability, this can damage the surface properties of the supraparticles and is not suitable for supraparticles containing organic components, thereby making stability a limitating factor for their application. In future research, researchers should further design the system by introducing active ingredients to form covalent bonds or using gel components to create a three-dimensional network between building blocks for limiting the domain of the supraparticles, thereby enhancing the stability to satisfy the mechanical strength requirements for practical applications.
IV. Many methods have been used for characterizing the structure and properties of supraparticles, such as scanning electron microscopy, confocal microscopy, fluorescence microscopy, goniometer, Brunauer-Emmer-Teller analysis, and home-built force-sensing systems. The lack of characterization standards makes it difficult to compare results, and therefore, standards must be established for evaluating the porosity and mechanical stability of supraparticles.
V. Detailed theoretical support remains lacking as the confinement-mediated particle assembly is a new method. In future developments, theoretical researchers need to participate in the theoretical simulation of the droplet confinement assembly process and develop a universal theoretical system based on the characteristics of the system for understanding and predicting the assembly process, interaction, and structural evolution of particles in evaporating droplets, thereby promoting the further developments and improvements in this field.

We hope that the overview of the fabrication principles and applications of supraparticles mediated by evaporating droplets on liquid-repellent surfaces presented in this review will help readers quickly capture the recent progress of this novel fabrication strategy in supraparticle production. We believe that droplet evaporation-mediated supraparticle fabrication will be widely accepted and applied. More theories and functional supraparticles will be developed from the fundamental research and practical applications through the researcher efforts.

CRediT authorship contribution statement

Xiaojing Wang: Writing – review & editing, Writing – original draft, Visualization, Formal analysis, Conceptualization. **Yuechang Lian:** Writing – review & editing, Writing – original draft, Visualization, Formal analysis, Conceptualization. **Siyuan Xiang:** Writing – review & editing, Writing – original draft, Visualization, Funding acquisition, Formal analysis, Conceptualization. **Shengyang Tao:** Writing – original draft. **Michael Kappl:** Writing – review & editing. **Wendong Liu:** Writing – review & editing, Writing – original draft, Supervision, Funding acquisition, Conceptualization.

Declaration of competing interest

The authors declare no competing financial interest.

Data availability

No data was used for the research described in the article.

Acknowledgments

W.L. acknowledges the National Science Foundation of China (NSFC) under Grant No. 22205031, the Natural Science Foundation of Liaoning Province under Grant No. 2022-MS-136, the Fundamental Research Funds for the Central Universities under Grant No. DUT21RC(3)078, and the Open Project of State Key Laboratory of Supramolecular Structure and Materials (sklssm2023012) for financial support. W.L. thanks Prof. Dr. Hans-Jürgen Butt for helpful discussions. S.X

acknowledges the Educational Commission of Liaoning Province of China (LJKMZ20220898), the Major Scientific and Technological Cooperation Funds of Zhoushan under Grant No. 2023C13012 for financial support.

References

[1] Bollhorst T, Jakob S, Köser J, Maas M, Rezwan K. Chitosan supraparticles with fluorescent silica nanoparticle shells and nanodiamond-loaded cores. J Mater Chem B 2017;5:1664–72.
[2] Faucon A, Maldiney T, Clément O, Hulin P, Nedellec S, Robard M, et al. Highly cohesive dual nanoassemblies for complementary multiscale bioimaging. J Mater Chem B 2014;2:7747–55.
[3] Xia Y, Tang Z. Monodisperse inorganic supraparticles: formation mechanism, properties and applications. Chem Commun 2012;48:6320–36.
[4] Uchida A, Kitayama Y, Takano E, Ooya T, Takeuchi T. Supraparticles comprised of molecularly imprinted nanoparticles and modified gold nanoparticles as a nanosensor platform. RSC Adv 2013;3:25306–11.
[5] Kim J, Hwang H, Butt H-J, Wooh S. Designing the shape of supraparticles by controlling the apparent contact angle and contact line friction of droplets. J Colloid Interface Sci 2021;588:157–63.
[6] Wintzheimer S, Reichstein J, Groppe P, Wolf A, Fett B, Zhou H, et al. Supraparticles for sustainability. Adv Funct Mater 2021;31:2011089.
[7] Kim Y-R, Lee TW, Park S, Jang J, Ahn C-W, Choi J-J, et al. Supraparticle engineering for highly dense microspheres: yttria-stabilized zirconia with adjustable micromechanical properties. ACS Nano 2021;15:10264–74.
[8] Gradon L, Balgis R, Hirano T, Rahmatika AM, Ogi T, Okuyama K. Advanced aerosol technologies towards structure and morphologically controlled next-generation catalytic materials. J Aerosol Sci 2020;149:105608.
[9] Ko Y-S, Joe YH, Seo M, Lim K, Hwang J, Woo K. Prompt and synergistic antibacterial activity of silver nanoparticle-decorated silica hybrid particles on air filtration. J Mater Chem B 2014;2:6714–22.
[10] Mattos BD, Tardy BL, Magalhães WLE, Rojas OJ. Controlled release for crop and wood protection: recent progress toward sustainable and safe nanostructured biocidal systems. J Control Release 2017;262:139–50.
[11] Zhou X, Li Z, Deng X, Yan B, Wang Z, Chen X, et al. High performance perovskite solar cells using Cu_9S_5 supraparticles incorporated hole transport layers. Nanotechnology 2019;30:445401.
[12] Vogel N, Retsch M, Fustin C-A, del Campo A, Jonas U. Advances in colloidal assembly: the design of structure and hierarchy in two and three dimensions. Chem Rev 2015;115:6265–311.
[13] Manoharan VN. Colloidal matter: packing, geometry, and entropy. Science 2015;349:1253751.
[14] Wintzheimer S, Granath T, Oppmann M, Kister T, Thai T, Kraus T, et al. Supraparticles: functionality from uniform structural motifs. ACS Nano 2018;12:5093–120.
[15] Zhuang J, Shaller AD, Lynch J, Wu H, Chen O, Li ADQ, et al. Cylindrical superparticles from semiconductor nanorods. J Am Chem Soc 2009;131:6084–5.
[16] Wang D, Xie T, Peng Q, Li Y. Ag, Ag_2S, and Ag_2Se nanocrystals: synthesis, assembly, and construction of mesoporous structures. J Am Chem Soc 2008;130:4016–22.
[17] Klajn R, Bishop KJM, Grzybowski BA. Light-controlled self-assembly of reversible and irreversible nanoparticle suprastructures. Proc Natl Acad Sci 2007;104:10305–9.
[18] Klajn R, Bishop KJM, Fialkowski M, Paszewski M, Campbell CJ, Gray TP, et al. Plastic and moldable metals by self-assembly of sticky nanoparticle aggregates. Science 2007;316:261–4.
[19] Maye MM, Lim IIS, Luo J, Rab Z, Rabinovich D, Liu T, et al. Mediator−template assembly of nanoparticles. J Am Chem Soc 2005;127:1519–29.
[20] Deans R, Ilhan F, Rotello VM. Recognition-mediated unfolding of a self-assembled polymeric globule. Macromolecules 1999;32:4956–60.
[21] Han J, Zhang X, Zhou Y, Ning Y, Wu J, Liang S, et al. Fabrication of CdTe nanoparticles-based superparticles for an improved detection of Cu^{2+} and Ag^{+}. J Mater Chem 2012;22:2679–86.
[22] Lu F, Cai W, Zhang Y. ZnO hierarchical micro/nanoarchitectures: solvothermal synthesis and structurally enhanced photocatalytic performance. Adv Funct Mater 2008;18:1047–56.
[23] Bai F, Wang D, Huo Z, Chen W, Liu L, Liang X, et al. A versatile bottom-up assembly approach to colloidal spheres from nanocrystals. Angew Chem Int Ed 2007;46:6650–3.
[24] Jenekhe SA, Chen XL. Self-assembled aggregates of rod-coil block copolymers and their solubilization and encapsulation of fullerenes. Science 1998;279:1903–7.
[25] Thayyil Raju L, Koshkina O, Tan H, Riedinger A, Landfester K, Lohse D, et al. Particle size determines the shape of supraparticles in self-lubricating ternary droplets. ACS Nano 2021;15:4256–67.
[26] Wang T, LaMontagne D, Lynch J, Zhuang J, Cao YC. Colloidal superparticles from nanoparticle assembly. Chem Soc Rev 2013;42:2804–23.
[27] Kim J, Shim W, Jo S-M, Wooh S. Evaporation driven synthesis of supraparticles on liquid repellent surfaces. J Ind Eng Chem 2021;95:170–81.
[28] Marín ÁG, Gelderblom H, Susarrey-Arce A, van Houselt A, Lefferts L, Gardeniers JGE, et al. Building microscopic soccer balls with evaporating colloidal fakir drops. Proc Natl Acad Sci 2012;109:16455–8.
[29] Rastogi V, Melle S, Calderón OG, García AA, Marquez M, Velev OD. Synthesis of light-diffracting assemblies from microspheres and nanoparticles in droplets on a superhydrophobic surface. Adv Mater 2008;20:4263–8.
[30] Sperling M, Velev OD, Gradzielski M. Controlling the shape of evaporating droplets by ionic strength: formation of highly anisometric silica supraparticles. Angew Chem Int Ed 2014;53:586–90.
[31] Tan H, Wooh S, Butt H-J, Zhang X, Lohse D. Porous supraparticle assembly through self-lubricating evaporating colloidal ouzo drops. Nat Commun 2019;10:478.
[32] Hu M, Butt H-J, Landfester K, Bannwarth MB, Wooh S, Thérien-Aubin H. Shaping the assembly of superparamagnetic nanoparticles. ACS Nano 2019;13:3015–22.
[33] Sefiane K. Patterns from drying drops. Adv Colloid Interface Sci 2014;206:372–81.
[34] Zhou J, Man X, Jiang Y, Doi M. Structure formation in soft-matter solutions induced by solvent evaporation. Adv Mater 2017;29:1703769.
[35] Sperling M, Papadopoulos P, Gradzielski M. Understanding the formation of anisometric supraparticles: a mechanistic look inside droplets drying on a superhydrophobic surface. Langmuir 2016;32:6902–8.
[36] Barrow SJ, Kasera S, Rowland MJ, del Barrio J, Scherman OA. Cucurbituril-based molecular recognition. Chem Rev 2015;115:12320–406.
[37] Deegan RD, Bakajin O, Dupont TF, Huber G, Nagel SR, Witten TA. Capillary flow as the cause of ring stains from dried liquid drops. Nature 1997;389:827–9.
[38] Gao A, Liu J, Ye L, Schönecker C, Kappl M, Butt H-J, et al. Control of droplet evaporation on oil-coated surfaces for the synthesis of asymmetric supraparticles. Langmuir 2019;35:14042–8.
[39] Still T, Yunker PJ, Yodh AG. Surfactant-induced marangoni eddies alter the coffee-rings of evaporating colloidal drops. Langmuir 2012;28:4984–8.
[40] Xu W, Ji M, Chen Y, Zheng H, Wang L, Peng D-L. Nickel colloidal superparticles: microemulsion-based self-assembly preparation and their transition from room-temperature superparamagnetism to ferromagnetism. J Phys Chem C 2021;125:5880–9.
[41] Mehanna YA, Sadler E, Upton RL, Kempchinsky AG, Lu Y, Crick CR. The challenges, achievements and applications of submersible superhydrophobic materials. Chem Soc Rev 2021;50:6569–612.
[42] Emelyanenko AM, Makvandi P, Moradialvand M, Boinovich LB. Harnessing extreme wettability: combatting spread of bacterial infections in healthcare. Surf Innov 2024;0:1–20.
[43] Hu DL, Prakash M, Chan B, Bush JWM. Water-walking devices. Exp Fluids 2007;43:769–78.
[44] Hu DL, Chan B, Bush JWM. The hydrodynamics of water strider locomotion. Nature 2003;424:663–6.
[45] Blossey R. Self-cleaning surfaces - virtual realities. Nat Mater 2003;2:301–6.
[46] Neinhuis C, Barthlott W. Characterization and distribution of water-repellent, self-cleaning plant surfaces. Ann Bot-Lond 1997;79:667–77.
[47] Wooh S, Butt H-J. A photocatalytically active lubricant-impregnated surface. Angew Chem Int Ed 2017;56:4965–9.
[48] Samaha MA, Gad-el-Hak M. Slippery surfaces: a decade of progress. Phys Fluids 2021;33:071301.
[49] Kim D, Lee M, Kim JH, Lee J. Dynamic contact angle measurements on lubricant infused surfaces. J Colloid Interface Sci 2021;586:647–54.
[50] Nirody JA, Jinn J, Libby T, Lee TJ, Jusufi A, Hu DL, et al. Geckos race across the water's surface using multiple mechanisms. Curr Biol 2018;28:4046–51.
[51] Bush JWM, Hu DL. Walking on water: biolocomotion at the interface. Annu Rev Fluid Mech 2006;38:339–69.
[52] Elzaabalawy A, Meguid SA. Advances in the development of superhydrophobic and icephobic surfaces. Int J Mech Mater Des 2022;18:509–47.
[53] Anand S, Paxson AT, Dhiman R, Smith JD, Varanasi KK. Enhanced condensation on lubricant-impregnated nanotextured surfaces. ACS Nano 2012;6:10122–9.
[54] Wong TS, Kang SH, Tang SKY, Smythe EJ, Hatton BD, Grinthal A, et al. Bioinspired self-repairing slippery surfaces with pressure-stable omniphobicity. Nature 2011;477:443–7.
[55] Sett S, Yan X, Barac G, Bolton LW, Miljkovic N. Lubricant-infused surfaces for low-surface-tension fluids: promise versus reality. ACS Appl Mater Interfaces 2017;9:36400–8.
[56] Drelich JW, Boinovich L, Chibowski E, Della Volpe C, Hołysz L, Marmur A, et al. Contact angles: history of over 200 years of open questions. Surf Innov 2020;8:3–27.
[57] Peppou-Chapman S, Hong JK, Waterhouse A, Neto C. Life and death of liquid-infused surfaces: a review on the choice, analysis and fate of the infused liquid layer. Chem Soc Rev 2020;49:3688–715.
[58] Maxwell JC. The scientific papers of James Clerk Maxwell. Cambridge: Cambridge University Press; 2011.
[59] Zhao Y, Shang L, Cheng Y, Gu Z. Spherical colloidal photonic crystals. Acc Chem Res 2014;47:3632–42.
[60] Syed A, Mangano L, Mao P, Han J, Song YA. Creating sub-50 nm nanofluidic junctions in a PDMS microchip via self-assembly process of colloidal silica beads for electrokinetic concentration of biomolecules. Lab Chip 2014;14:4455–60.
[61] Layani M, Gruchko M, Milo O, Balberg I, Azulay D, Magdassi S. Transparent conductive coatings by printing coffee ring arrays obtained at room temperature. ACS Nano 2009;3:3537–42.
[62] Langmuir I. The evaporation of small spheres. Phys Ther Rev 1918;12:368–70.
[63] Ramos SMM, Dias JF, Canut B. Drop evaporation on superhydrophobic PTFE surfaces driven by contact line dynamics. J Colloid Interface Sci 2015;440:133–9.
[64] Picknett RG, Bexon R. The evaporation of sessile or pendant drops in still air. J Colloid Interface Sci 1977;61:336–50.

[65] Bigdeli MB, Tsai PA. Making photonic crystals via evaporation of nanoparticle-laden droplets on superhydrophobic microstructures. Langmuir 2020;36:4835–41.
[66] Jokinen V, Sainiemi L, Franssila S. Complex droplets on chemically modified silicon nanograss. Adv Mater 2008;20:3453–6.
[67] Chen X, Ma R, Li J, Hao C, Guo W, Luk BL, et al. Evaporation of droplets on superhydrophobic surfaces: surface roughness and small droplet size effects. Phys Rev Lett 2012;109:116101.
[68] Bussonnière A, Bigdeli MB, Chueh D-Y, Liu Q, Chen P, Tsai PA. Universal wetting transition of an evaporating water droplet on hydrophobic micro- and nano-structures. Soft Matter 2017;13:978–84.
[69] Yu Y-S, Wang Z, Zhao Y-P. Experimental and theoretical investigations of evaporation of sessile water droplet on hydrophobic surfaces. J Colloid Interface Sci 2012;365:254–9.
[70] Aldhaleai A, Khan F, Thundat T, Tsai PA. Evaporation dynamics of water droplets on superhydrophobic nanograss surfaces. Int J Heat Mass Tran 2020;160:120149.
[71] McHale G, Aqil S, Shirtcliffe NJ, Newton MI, Erbil HY. Analysis of droplet evaporation on a superhydrophobic surface. Langmuir 2005;21:11053–60.
[72] Reyssat M, Yeomans JM, Quéré D. Impalement of fakir drops. EPL 2008;81:26006.
[73] Choi C-H, Kim C-JC. Droplet evaporation of pure water and protein solution on nanostructured superhydrophobic surfaces of varying heights. Langmuir 2009;25:7561–7.
[74] Misyura SY. The anomalously high rate of crystallization, controlled by crystal forms under the conditions of a limited liquid volume. Cryst Growth Des 2018;18:1327–38.
[75] Misyura SY, Morozov VS, Egorov RI. Water evaporation on structured surfaces with different wettability. Int J Heat Mass Tran 2022;192:122843.
[76] Gross M, Varnik F, Raabe D, Steinbach I. Small droplets on superhydrophobic substrates. Phys Rev E 2010;81:051606.
[77] Xu W, Leeladhar R, Kang YT, Choi C-H. Evaporation kinetics of sessile water droplets on micropillared superhydrophobic surfaces. Langmuir 2013;29:6032–41.
[78] Anantharaju N, Panchagnula M, Neti S. Evaporating drops on patterned surfaces: transition from pinned to moving triple line. J Colloid Interface Sci 2009;337:176–82.
[79] Liu W, Midya J, Kappl M, Butt H-J, Nikoubashman A. Segregation in drying binary colloidal droplets. ACS Nano 2019;13:4972–9.
[80] Li Y, Diddens C, Segers T, Wijshoff H, Versluis M, Lohse D. Evaporating droplets on oil-wetted surfaces: suppression of the coffee-stain effect. Proc Natl Acad Sci 2020;117:16756–63.
[81] Tan H, Diddens C, Versluis M, Butt H-J, Lohse D, Zhang X. Self-wrapping of an ouzo drop induced by evaporation on a superamphiphobic surface. Soft Matter 2017;13:2749–59.
[82] Mistura G, Pierno M. Drop mobility on chemically heterogeneous and lubricant-impregnated surfaces. Adv Phys -X 2017;2:591–607.
[83] Smith JD, Dhiman R, Anand S, Reza-Garduno E, Cohen RE, McKinley GH, et al. Droplet mobility on lubricant-impregnated surfaces. Soft Matter 2013;9:1772–80.
[84] Zhang BJ, Kim KJ, Lee CY. Behavior of an evaporating water droplet on lubricant-impregnated nano-structured surface. Exp Therm Fluid Sci 2018;96:216–23.
[85] Dash S, Garimella SV. Droplet evaporation dynamics on a superhydrophobic surface with negligible hysteresis. Langmuir 2013;29:10785–95.
[86] Marín ÁG, Gelderblom H, Lohse D, Snoeijer JH. Order-to-disorder transition in ring-shaped colloidal stains. Phys Rev Lett 2011;107:085502.
[87] Eggers J, Pismen LM. Nonlocal description of evaporating drops. Phys Fluids 2010;22:112101.
[88] Wooh S, Huesmann H, Tahir MN, Paven M, Wichmann K, Vollmer D, et al. Synthesis of mesoporous supraparticles on superamphiphobic surfaces. Adv Mater 2015;27:7338–43.
[89] TJ J Orava, Parkkinen J, Leppanen V-P. Colloids Res Appl 2007:32.
[90] Hilden JL, Trumble KP. Numerical analysis of capillarity in packed spheres: planar hexagonal-packed spheres. J Colloid Interface Sci 2003;267:463–74.
[91] Henson WA, Taber DA, Bradford EB. Mechanism of film formation of latex paint. Ind Eng Chem Res 1953;45:735–9.
[92] Rastogi V, García AA, Marquez M, Velev OD. Anisotropic particle synthesis inside droplet templates on superhydrophobic surfaces. Macromol Rapid Commun 2010;31:190–5.
[93] Liu W, Kappl M, Steffen W, Butt H-J. Controlling supraparticle shape and structure by tuning colloidal interactions. J Colloid Interface Sci 2022;607:1661–70.
[94] Liu W, Kappl M, Butt H-J. Tuning the porosity of supraparticles. ACS Nano 2019;13:13949–56.
[95] Timonen JVI, Latikka M, Leibler L, Ras RHA, Ikkala O. Switchable static and dynamic self-assembly of magnetic droplets on superhydrophobic surfaces. Science 2013;341:253–7.
[96] Sperling M, Spiering VJ, Velev OD, Gradzielski M. Controlled formation of patchy anisometric fumed silica supraparticles in droplets on bent superhydrophobic surfaces. Part Part Syst Charact 2017;34:1600176.
[97] Oguztürk HE, Bauer LJ, Mantouvalou I, Kanngiβeer B, Velev OD, Gradzielski M. Preparation of reinforced anisometric patchy supraparticles for self-propulsion. Part Part Syst Charact 2021;38:2000328.
[98] Al Harraq A, Bharti B. Increasing aspect ratio of particles suppresses buckling in shells formed by drying suspensions. Soft Matter 2020;16:9643–7.
[99] Seyfert C, Berenschot EJW, Tas NR, Susarrey-Arce A, Marin A. Evaporation-driven colloidal cluster assembly using droplets on superhydrophobic fractal-like structures. Soft Matter 2021;17:506–15.
[100] Shim W, Moon CS, Kim H, Kim HS, Zhang H, Kang SK, et al. Tailoring the morphology of supraparticles by primary colloids with different shapes, sizes and dispersities. Crystals 2021;11:79.
[101] Zhou J, Yang J, Gu Z, Zhang G, Wei Y, Yao X, et al. Controllable fabrication of noniridescent microshaped photonic crystal assemblies by dynamic three-phase contact line behaviors on superhydrophobic substrates. ACS Appl Mater Interfaces 2015;7:22644–51.
[102] Al-Shehri H, Horozov TS, Paunov VN. Preparation and attachment of liquid-infused porous supra-particles to liquid interfaces. Soft Matter 2016;12:8375–87.
[103] Butt Hans-Jurgen, Kappl Michael. Van der Waals forces. Surface and interfacial forces. 2018. p. 5–53.
[104] Boinovich L, Emelyanenko A. Principles of design of superhydrophobic coatings by deposition from dispersions. Langmuir 2009;25:2907–12.
[105] Hunter RJ. Foundations of colloids science. Oxford university Press; 2001.
[106] Fernández-Barbero A, Martın-Rodrıguez A, Callejas-Fernández J, Hidalgo-Alvarez R. On the calculation of electrokinetic potential and hamaker constant of model colloids. J Colloid Interface Sci 1994;162:257–60.
[107] Ohshima H. Electrostatic interaction between two dissimilar spheres: an explicit analytic expression. J Colloid Interface Sci 1994;162:487–95.
[108] Derjaguin BV, Churaev NV, Muller VM. Surface forces. New York: Consultants Bureau; 1987.
[109] Cross NL, Picknett RG. Particle adhesion in the presence of a liquid film. In: Johnson HR, Littler DJ, editors. International conference on the mechanism of corrosion by fuel impurities. Marchwood, England: Butterworths; 1963. p. 383–90.
[110] Adams MJPV. The cohesive forces between particles with interstitial liquid. IChemE Symposium Ser 1985:147–60.
[111] O. R.. On the theory of lubrication and its application to Mr beauchamps tower's experiments, including an experimental detemination of the viscosity of olive oil. Philos Trans R Soc Lond A 1886;177:157–234.
[112] Sekido T, Wooh S, Fuchs R, Kappl M, Nakamura Y, Butt H-J, et al. Controlling the structure of supraballs by pH-responsive particle assembly. Langmuir 2017;33:1995–2002.
[113] Cichocki B, Felderhof BU. Long-time self-diffusion coefficient and zero-frequency viscosity of dilute suspensions of spherical brownian particles. J Chem Phys 1988;89:3705–9.
[114] Jiao L, Tong J, Wu Y, Hu Y, Wu H, Li D, et al. Self-assembly of supraparticles on a lubricated-superamphiphobic patterned surface. Appl Surf Sci 2022;576:151684.
[115] Heo J, Lee J, Shim W, Kim H, Fujii S, Lim J, et al. Evaporation-driven supraparticle synthesis by self-lubricating colloidal dispersion microdrops. ACS Appl Mater Interfaces 2023;15:38986–95.
[116] Mattos BD, Greca LG, Tardy BL, Magalhães WLE, Rojas OJ. Green formation of robust supraparticles for cargo protection and hazards control in natural environments. Small 2018;14:1801256.
[117] Jo S-M, Kim J, Lee JE, Wurm FR, Landfester K, Wooh S. Multimodal enzyme-carrying suprastructures for rapid and sensitive biocatalytic cascade reactions. Adv Sci 2022;9:2104884.
[118] Kang S, Wang W, Rahman A, Nam W, Zhou W, Vikesland PJ. Highly porous gold supraparticles as surface-enhanced Raman spectroscopy (SERS) substrates for sensitive detection of environmental contaminants. RSC Adv 2022;12:32803–12.
[119] Cao J, Huang Y, Shang Z, Liu X, Lu C, Chen H, et al. Fabrication of core shell Au@Ag supraparticles with 3D hotspots via evaporation self-assembly for sensitive surface enhanced Raman scattering detection. Sens Actuators B 2023;382:133529.
[120] Song J, Cheng W, Nie M, He X, Nam W, Cheng J, et al. Partial leidenfrost evaporation-assisted ultrasensitive surface-enhanced raman spectroscopy in a janus water droplet on hierarchical plasmonic micro−/nanostructures. ACS Nano 2020;14:9521–31.
[121] Wang Y, Wise AK, Tan J, Maina JW, Shepherd RK, Caruso F. Mesoporous silica supraparticles for sustained inner-ear drug delivery. Smal 2014;10:4244–8.
[122] Huang Y, Zhou J, Su B, Shi L, Wang J, Chen S, et al. Colloidal photonic crystals with narrow stopbands assembled from low-adhesive superhydrophobic substrates. J Am Chem Soc 2012;134:17053–8.
[123] Lim CH, Kang H, Kim S-H. Colloidal assembly in leidenfrost drops for noniridescent structural color pigments. Langmuir 2014;30:8350–6.
[124] Zhao B, Borghei M, Zou T, Wang L, Johansson L-S, Majoinen J, et al. Lignin-based porous supraparticles for carbon capture. ACS Nano 2021;15:6774–86.
[125] Shan J, Zhang Y, Wang J, Ren T, Jin M, Wang X. Microextraction based on microplastic followed by SERS for on-site detection of hydrophobic organic contaminants, an indicator of seawater pollution. J Hazard Mater 2020;400:123202.
[126] Huang T-Y, Huang G-L, Zhang C-Y, Zhuang B-W, Liu B-X, Su L-Y, et al. Supramolecular photothermal nanomedicine mediated distant tumor inhibition via PD-1 and TIM-3 blockage. Front Chem 2020;8:1.
[127] Lai H, Dai H, Li G, Zhang Z. Rapid determination of pesticide residues in fruit and vegetable using Au@AgNPs decorated 2D Ni-MOF nanosheets as efficient surface-enhanced Raman scattering substrate. Sens Actuators B 2022;369:132360.
[128] Zhizhchenko A, Kuchmizhak A, Vitrik O, Kulchin Y, Juodkazis S. On-demand concentration of an analyte on laser-printed polytetrafluoroethylene. Nanoscale 2018;10:21414–24.
[129] Liu K, Bai Y, Zhang L, Yang Z, Fan Q, Zheng H, et al. Porous Au–Ag nanospheres with high-density and highly accessible hotspots for SERS analysis. Nano Lett 2016;16:3675–81.
[130] Stoerzinger KA, Lin JY, Odom TW. Nanoparticle SERS substrates with 3D raman-active volumes. Chem Sci 2011;2:1435–9.

[131] Phan-Quang GC, Han X, Koh CSL, Sim HYF, Lay CL, Leong SX, et al. Three-dimensional surface-enhanced raman scattering platforms: large-scale plasmonic hotspots for new applications in sensing, microreaction, and data storage. Acc Chem Res 2019;52:1844–54.
[132] AshaRani PV, Low Kah Mun G, Hande MP, Valiyaveettil S. Cytotoxicity and genotoxicity of silver nanoparticles in human cells. ACS Nano 2009;3:279–90.
[133] Norris DJ. A view of the future. Nat Mater 2007;6:177–8.
[134] Prevo BG, Fuller JC, Velev OD. Rapid deposition of gold nanoparticle films with controlled thickness and structure by convective assembly. Chem Mater 2005;17:28–35.
[135] Hynninen A-P, Thijssen JHJ, Vermolen ECM, Dijkstra M, van Blaaderen A. Self-assembly route for photonic crystals with a bandgap in the visible region. Nat Mater 2007;6:202–5.
[136] Sperling M, Gradzielski M. Droplets, evaporation and a superhydrophobic surface: simple tools for guiding colloidal particles into complex materials. Gels 2017;32:15.